TU Delft

Delft University of Technology

Document Version
Final published version

Licence
CC BY

Citation (APA)
Liang, X., Chen, J., Dong, H., Li, Z., Liu, C., & Ye, G. (2026). One-part binders from woody biomass fly ash and blast furnace slag: reaction mechanisms and microstructural evolution. *Cement and Concrete Research*, *205*, Article 108227. https://doi.org/10.1016/j.cemconres.2026.108227

Important note
To cite this publication, please use the final published version (if applicable).
Please check the document version above.

Copyright
In case the licence states “Dutch Copyright Act (Article 25fa)”, this publication was made available Green Open Access via the TU Delft Institutional Repository pursuant to Dutch Copyright Act (Article 25fa, the Taverne amendment). This provision does not affect copyright ownership.
Unless copyright is transferred by contract or statute, it remains with the copyright holder.

Sharing and reuse
Other than for strictly personal use, it is not permitted to download, forward or distribute the text or part of it, without the consent of the author(s) and/or copyright holder(s), unless the work is under an open content license such as Creative Commons.

Takedown policy
Please contact us and provide details if you believe this document breaches copyrights.
We will remove access to the work immediately and investigate your claim.

This work is downloaded from Delft University of Technology.

Cement and Concrete Research 205 (2026) 108227

Contents lists available at ScienceDirect

Cement and Concrete Research

journal homepage: www.elsevier.com/locate/cemconres

One-part binders from woody biomass fly ash and blast furnace slag: reaction mechanisms and microstructural evolution

Xuhui Liang [a,*], Jiayi Chen [a], Hua Dong [a], Zhenming Li [b], Chen Liu [a], Guang Ye [a,c,**]

[a] Microlab, Faculty of Civil Engineering and Geoscience, Delft University of Technology, Delft, the Netherlands
[b] School of Civil and Environmental Engineering, Harbin Institute of Technology, China
[c] Magnel Laboratory for Concrete Research, Department of Structural Engineering, Ghent University, Ghent, Belgium

ARTICLE INFO

Keywords:
Woody biomass fly ash
Hydration mechanism
Microstructure evolution
Cement-free binders
Thermodynamic modelling

ABSTRACT

Woody biomass fly ash (WBFA) is the main by-product of woody biomass energy production. However, its use in cementitious materials remains limited due to its low intrinsic reactivity, largely associated with the scarcity of aluminosilicate phases. At the same time, the high alkalinity and sulphur content in WBFA make it a promising component for formulating cement-free binders without additional chemical activators, when combined with highly reactive precursors. This study investigates the reaction mechanisms and microstructural evolution of binders based on WBFA and ground granulated blast furnace slag (BFS), with the aim of elucidating their synergistic interactions and optimizing performance. Binary pastes with varying WBFA/BFS ratios mixed with water were prepared and characterized by isothermal calorimetry, pore solution analysis, XRD, FTIR, TGA, SEM-EDS, and MIP. The results show that, although increasing WBFA content initially delayed hydration by limiting the dissolution of reactive species, it markedly enhances long-term reactivity and strength through sustained release of alkali and sulphate. The main hydration products are C-(A)-S-H gels, ettringite, Friedel's salt, and hydrotalcite, with their amount and assemblage strongly governed by the WBFA/BFS ratio. Reaction kinetics analysis and thermodynamic modelling confirm the dual role of WBFA as both a reactive precursor and internal alkali/sulphate activator. Among the formulations studied, the mixture with a WBFA/BFS ratio of 50:50 exhibited the best overall performance, achieving the highest compressive strength and lowest porosity. These findings clarify the reaction mechanisms in WBFA-BFS binary pastes, providing practical guidance for designing WBFA-based, cement-free binders for sustainable construction applications.

1. Introduction

Over the past few decades, the global energy landscape has undergone a rapid transition from fossil fuel-based systems to renewable energy sources. Among these, biomass energy has emerged as a significant contributor to sustainable energy. In particular, wood biomass derived from both virgin wood and post-service wood products, e.g., demolition timber from construction and furniture waste, has become a major feedstock for biomass energy [1]. In the EU, wood biomass accounts for more than 70% of the energy generated from biofuels [2], largely due to its favourable characteristics as a renewable resource with a carbon-neutral profile [3].

Electricity generation from woody biomass, primarily through the incineration process, is increasingly being adopted as a substitute for conventional coal-fired power plants [4,5]. However, this process generates substantial quantities of WBFA as a by-product, the accumulation of which has escalated in recent years. According to the estimates in [6], global annual wood biomass production is approximately 1.02 billion tons, generating about 15.21 million tons of ash each year. The effective management and valorisation of WBFA have thus become both an environmental imperative and a technological challenge.

Given the rising demand for raw materials in the construction industry, WBFA presents a promising alternative resource. Despite variations in feedstock and combustion techniques that may affect the composition of WBFA, most of WBFA is reported consistently with high content of CaO (~40%) and SiO_2 (~20%), together with other components including K_2O (~10%), Al_2O_3 (~5%), and SO_3 (~4%) [7]. This Ca-Si-Al-Na(K)-S composition closely aligns with the key constituents of

* Corresponding author.
** Correspondence to: G. Ye, Microlab, Faculty of Civil Engineering and Geoscience, Delft University of Technology, Delft, the Netherlands.
E-mail addresses: x.liang@alu.cqu.edu.cn (X. Liang), g.ye@tudelft.nl (G. Ye).

https://doi.org/10.1016/j.cemconres.2026.108227
Received 14 January 2026; Received in revised form 12 March 2026; Accepted 31 March 2026
Available online 13 April 2026
0008-8846/© 2026 The Author(s). Published by Elsevier Ltd. This is an open access article under the CC BY license (http://creativecommons.org/licenses/by/4.0/).

cementitious materials, which has prompted investigations into the potential use of WBFA in developing cementitious materials. However, compared to the conventional supplementary cementitious materials (SCMs), e.g., BFS and coal fly ash (CFA), WBFA contains a relatively low aluminosilicate fraction (typically about 20–40%) and is mineralogically dominated by crystalline phases; therefore, its pozzolanic reactivity is reported to be much lower [8,9]. Consequently, blended cements incorporating WBFA typically exhibit inferior mechanical performance compared with those containing BFS or CFA at equivalent cement replacement levels. Accordingly, the recommended substitution ratio for WBFA as a cement replacement is usually restricted to 5–10% [10].

Beyond its role as a SCM, WBFA has also been explored as a precursor for alkali-activated materials (AAMs). Under highly alkaline conditions, WBFA dissolution is significantly enhanced relative to its dissolution in blended cements, allowing greater extraction of calcium, silicon, and aluminium for the formation of reaction products [11]. However, when used as the sole precursor, the intrinsically low reactivity of WBFA demands a highly alkaline environment to promote the dissolution and depolymerisation of the aluminosilicate network, enabling the release of reactive silicate and aluminate species [11,12]. For example, NaOH concentrations up to 18 M have been reported in the development of WBFA-based AAMs [13], which raises concerns regarding practicality and safety. It is therefore more feasible to develop WBFA-containing AAMs in combination with highly reactive precursors, allowing WBFA to serve as a partial rather than primary component [14,15]. Nonetheless, the proportion of WBFA as a precursor in AAMs development remains moderate, improving its utilization within such binder systems remains a challenge.

Recent studies have suggested that the intrinsic alkalis and sulphur present in WBFA may play a more active role in binder systems than previously recognised. Minerals such as sylvite (KCl), aphthitalite ($(K, Na)_3Na(SO_4)_2$), and syngenite ($K_2Ca(SO_4)_3$) have been widely reported in WBFA [7,16], which might be effective in promoting the reaction of precursors in AAMs. Jurado-Contreras et al. [17] found that the waterglass-activated WBFA-metakaolin AAMs synthesized using raw WBFA exhibited higher strength than those incorporating washed WBFA, in which soluble alkalis and sulphur had been largely removed. This suggested that the inherent alkalis and sulphur in WBFA may act as internal activators promoting the reaction of precursors. Similar concepts, involving the utilization of alkalis originating from solid wastes to initiate or enhance alkali-activated reactions, have been widely reported in the literature [18–20]. Building on this concept, our previous proof-of-concept study demonstrated the feasibility of a cement-free binder produced by directly mixing WBFA and BFS with water, without the addition of external alkalis or chemical activators [12]. The paste exhibited satisfactory mechanical properties and workability with the aid of superplasticizers. Although preliminary characterization confirmed the viability of this binder system, the underlying reaction mechanisms, particularly the microstructural development and strength evolution, remain insufficiently understood. Key questions regarding how WBFA influences the hydration of BFS and how varying WBFA proportions affect the reaction kinetics of the binders remain gaps for further investigations.

The present study aims to elucidate the reaction mechanisms of WBFA–BFS cement-free binder. Binary pastes with varying WBFA-to-BFS ratios were prepared, and their reaction processes, hydrates formation, microstructural evolution were comprehensively investigated. Insights gained from this study are expected to inform the rational design of cement-free binder formulations, facilitating more effective utilization of WBFA in sustainable construction materials.

2. Materials and methods

2.1. Materials

WBFA was collected from a Dutch biomass power plant. The feedstock consisted of a mixture of wood chips, pruning wood, scrap wood, and paper sludge. The wood biomass was combusted in a bubbling fluidized bed boiler operating at temperature up to 900 °C. After which the WBFA was captured using bag filters. Prior to use in this study, the raw WBFA underwent a pretreatment process to remove metallic aluminium and free lime, following the procedure described in [12]. Unless otherwise specified, WBFA discussed here refers to this treated material. BFS was obtained from Ecocem B.V. (the Netherlands).

The chemical compositions of raw materials determined by XRF are shown in Table 1, while the mineral phases identified by XRD are shown in Fig. 1. The quantitative mineral composition of WBFA determined by QXRD was previously reported in [12]. The chemical composition of its amorphous phase was estimated through a mass balance approach by subtracting the chemical compositions of crystalline minerals through QXRD from the bulk composition determined by XRF, as detailed in Table A1.

WBFA used in this study is abundant in calcium, potassium, silicon, and sulphur. For comparison, $WBFA_{mean}$ in Table 1 represents the mean chemical composition of approximately 97 WBFA samples reported in the literature from various feedstocks. The close agreement between these values indicates that the ash used in this work is representative of the typical composition of WBFA. The main crystalline phases are portlandite, quartz, calcite, Fridel's salt and alkali-(calcium) sulphates, which are commonly reported phases in WBFA [21]. The particle size distribution of WBFA and BFS measured by diffraction laser was shown in Fig. 2.

2.2. Experimental methods

2.2.1. Mixture proportions

In this study, WBFA-BFS binary pastes were formulated with varying WBFA to BFS ratios, namely B30S70, B50S50, and B70S30, to investigate the reaction kinetics, microstructure evolution, and compressive strength. Single-component pastes composed of pure WBFA (B100S0) and pure BFS (B0S100) did not develop sufficient strength for demoulding and therefore were only included as reference samples in the isothermal calorimetry test to facilitate comparison with the binary mixtures. The water-to-binder ratio (W/B) was fixed at 0.40 to ensure adequate workability for sample casting (Table 2).

2.2.2. Isothermal calorimetry

An isothermal calorimetry test was conducted to investigate the reaction kinetics of the pastes. The experiments were carried out using a TAM-Air-314 isothermal conduction calorimeter. A calibration program was performed at a temperature of 20 °C for at least 24 h before the experiments. During the test, pastes were prepared by hand-mixing, approximately 7 g of fresh paste were used for each measurement. A fixed amount of sand with a heat capacity equivalent to that of the pastes, was used as reference. Given the slow reaction of WBFA-BFS pastes, the test was carried out for 14 days.

2.2.3. Pore solution

The chemical compositions of pore solution were measured to investigate the reaction process of binary pastes. Fresh pastes were cast into cylindrical polyethylene bottles with a diameter of 35 mm and a height of 70 mm, sealed tightly and cured at 20 °C for 1 day, 7 days, 14 days, and 28 days prior to pore solution extraction.

Pore solutions were extracted using the steel-die method [22]. Specimens were subjected to a gradually increasing load by a high-pressure device up to 250 MPa, to express the pore solutions. After collection, the pore solutions were vacuum filtered to remove the

Table 1
Primary chemical compositions (in wt%) of WBFA and BFS determined by XRF.

	SiO_2	Al_2O_3	CaO	Fe_2O_3	SO_3	Na_2O	K_2O	Cl	MgO	LOI (1000 °C)
WBFA	15.20	4.06	43.65	2.58	6.0	1.72	6.92	3.18	3.33	6.03
BFS	31.77	13.25	40.50	0.52	1.49	0.12	0.34	–	9.27	1.31
$WBFA_{mean}$ [7]	21.88	5.19	37.61	2.59	4.44	1.36	10.07	1.69	4.78	n/a

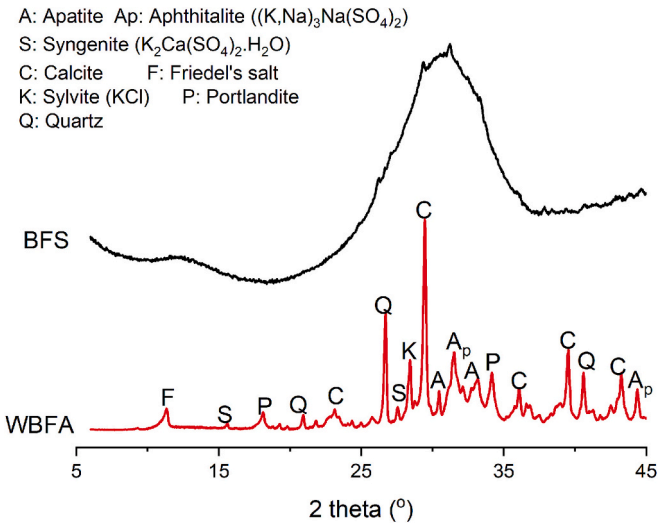

Fig. 1. XRD patterns of raw materials.

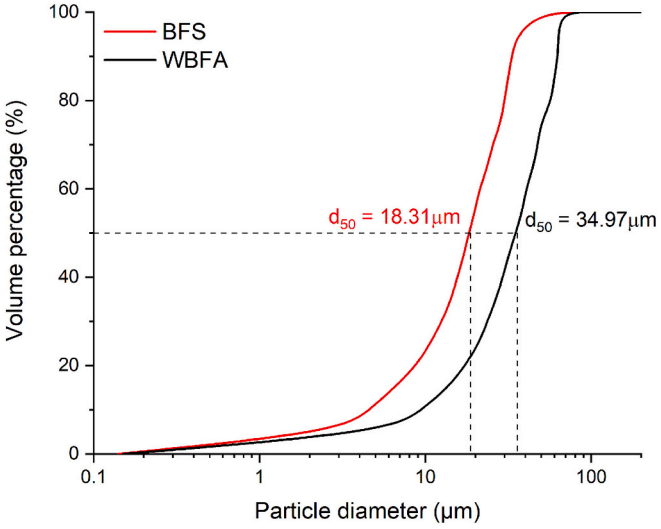

Fig. 2. Particle size distribution of raw materials.

Table 2
Mixture proportions of pastes.

Groups	WBFA (wt%)	BFS (wt%)	Water to binder ratio** (W/B)
B0S100*	0	100	0.40
B30S70	30	70	
B50S50	50	50	
B70S30	70	30	
B100S0*	100	0	

* These mixtures were only investigated in isothermal calorimetry.
** Binder = WBFA + BFS.

retained particles. The concentrations of OH^- were determined by titration against hydrochloric acid (0.1 M) with a phenolphthalein indicator. The concentration of chloride was determined by Mohr's method [23,24]. The remaining pore solutions were acidified by HNO_3 solutions, diluted, and then analysed for the concentrations of Ca, Si, Al, K, S, Na by Inductively Coupled Plasma Optical Emission Spectroscopy (ICP-OES). The relative standard deviation of the ICP-OES measurements for each element was within 5%.

2.2.4. Reaction products characterization

- Sample preparation

Before test, samples underwent a hydration stoppage program to ensure preservation of the hydration at a designated time. The hydration stoppage of specimens was carried out by solvent exchange methods as suggested by Snelling et al. [25]. Samples were immersed in isopropanol and manually crushed into fines with a pestle. Afterwards, the crushed samples were immersed in isopropanol for 15 min and then filtered. Residuals were rinsed with diethyl ether, followed by oven drying at 40 °C for about 8 min to facilitate the evaporation of the organic solvents. The dried samples were then collected and subjected to characterization. Samples cured for 7, 28, and 60 days were prepared accordingly.

- X-ray diffraction (XRD) test

XRD was conducted to identify the crystalline phases in the binary pastes. A Bruker D8 Advance diffractometer with Cu Kα radiation was used to perform the measurements. The operating voltage and current were set at 45 kV and 40 mA, respectively. The diffraction scanning of 2θ ranges from 5 to 70° with a counting speed of 0.01 °/s.

- Fourier-transform infrared spectroscopy (FTIR)

FTIR was applied to investigate the evolution of the chemical bonds of pastes during the hydration process. The measurements were performed using a Spectrum™ 100 Optical ATR-FTIR spectrometer. The scanning range was 600–4000 cm^{-1} with a resolution of 4 cm^{-1}. An average of 20 scans were collected to obtain reliable spectra.

- Thermogravimetric analysis (TGA)

TGA was used as a semi-quantification tool for analysing the contents of hydrates in the pastes. The test was operated with a NETZSCH STA 449 F3 Jupiter instrument. An argon atmosphere was employed with a temperature range from 40 to 1000 °C and a heating rate of 10 °C/min. Approximately 30 mg of powder samples was used for each measurement.

2.2.5. Microstructure characterization

- Mercury Intrusion Porosimetry (MIP)

MIP was performed to determine the pore structure evolution of the pastes at 7, 28, and 60 days. Initially, specimens were sawed into small fragments and immersed in isopropanol for approximately 5 days, with the solvent renewed every day. Afterwards, samples were freeze-dried to

facilitate the removal of isopropanol, rendering them ready for testing. An AutoPore IV mercury porosimeter was used with a mercury contact angle of 141° and a surface tension of 480 mN/m. The intrusion process consisted of a low-pressure program ranging from 0 to 0.14 MPa and a high-pressure program ranging from 0.14 to 210 MPa. The pore diameter was then determined by the Washburn equation, which correlates pore diameter with pressure [26].

- Scanning electron microscopy (SEM) coupled with electron dispersive spectroscopy (EDS)

Backscattered electron (BSE) imaging was used for microstructure characterization to better identify phases through distinct greyscale variation, mainly influenced by the atomic number [27]. The analysis was conducted on samples cured for 7 and 60 days. Before experiments, the freeze-dried samples, as illustrated in MIP sample preparation, were impregnated with a low viscosity epoxy resin, then subjected to grinding and polishing down to 0.25 μm. Finally, the well-polished samples were carbon-coated and prepared for test.

A FEI QUANTA FEG 650 ESEM (Thermo Fisher Scientific), equipped with a solid-state EDS detector, was used under high vacuum mode. The working voltage was set at 15 kV and the working distance was 10 mm [28].

2.2.6. Compressive strength

The compressive strength of binary pastes was measured using cubic specimens with a dimension of 4 cm. The fresh pastes were firstly sealed cured for 3 days before demoulding, subsequently cured in the fog room at a temperature of 20 °C and RH above 95% until the compressive strength test. The compressive strength of pastes was measured at 7, 28, and 60 days, with the average value obtained from six samples for each stage.

3. Results

3.1. Heat evolution

Fig. 3 shows the normalized heat flow of pastes with varying WBFA-to-BFS ratios. The first exothermal peak appears immediately once the pastes are placed in the calorimeter chamber. It is generally accepted that this peak is mainly reflects the wetting and dissolution of raw materials [29,30]. Beyond this peak, no additional exothermic peak is observed in the single-component pastes (B0S100 and B100S0), suggesting their limited reaction. In the contrary, the binary pastes exhibit additional exothermic peaks at later ages, which implies that more intensive reactions occur in the binary pastes, leading to the generation of a substantial amount of reaction products.

The heat flow curves of the binary pastes, in general, represents the multi-stage reaction comparable to slag-rich binder [31]. To clarify the reaction process, besides the wetting and dissolution-introduced thermal peak, three other distinguishable stages can be identified in the binary pastes:

- Dormant period

The dormant period follows the end of the first main peak. During this period, the heat flow remains low for a short duration. By amplifying the exothermic heat flow curves of binary pastes in the first 8 h, it is observed that the dormant period comes earlier with a shorter duration in pastes with a lower WBFA/BFS ratio with the occurrence of an earlier onset of the acceleration stage.

- Acceleration and deceleration periods

Following the dormant period, the main exothermal peaks (acceleration and deceleration stages) are observed in binary mixtures and correspond to the large amounts of hydrates formation. It is interesting to note that with the increasing WBFA/BFS ratios, the pastes display a clear second wave or shoulder close to the main peak, which is similar to the hydration characteristics of slag cement [32]. Given the high amount of sulfate in WBFA, it is reasonable to infer that the wave is associated with the precipitation of ettringite [33,34]. Increasing WBFA/BFS ratios results in a larger amount of sulfate in the pastes, promoting the formation of ettringite and therefore, the broadening of the second main peak in mixture with higher WBFA content.

- Steady period

The steady stage follows the end of the deceleration period, during which the reaction rate of pastes gradually decreases to a low extent while maintaining a mild reaction. Mixtures with a higher WBFA/BFS ratio show greater heat flow, indicating a more intense reaction. This can be attributed to the continuous supply of alkalis, sulphate, and portlandite from WBFA, which promotes the reaction of BFS during the later hydration stages.

In general, the normalized cumulative heat curves (Fig. 3(b)) show that, mixtures with more WBFA content exhibit greater cumulative heat release within the first 12 h, reflecting more intensive initial dissolution

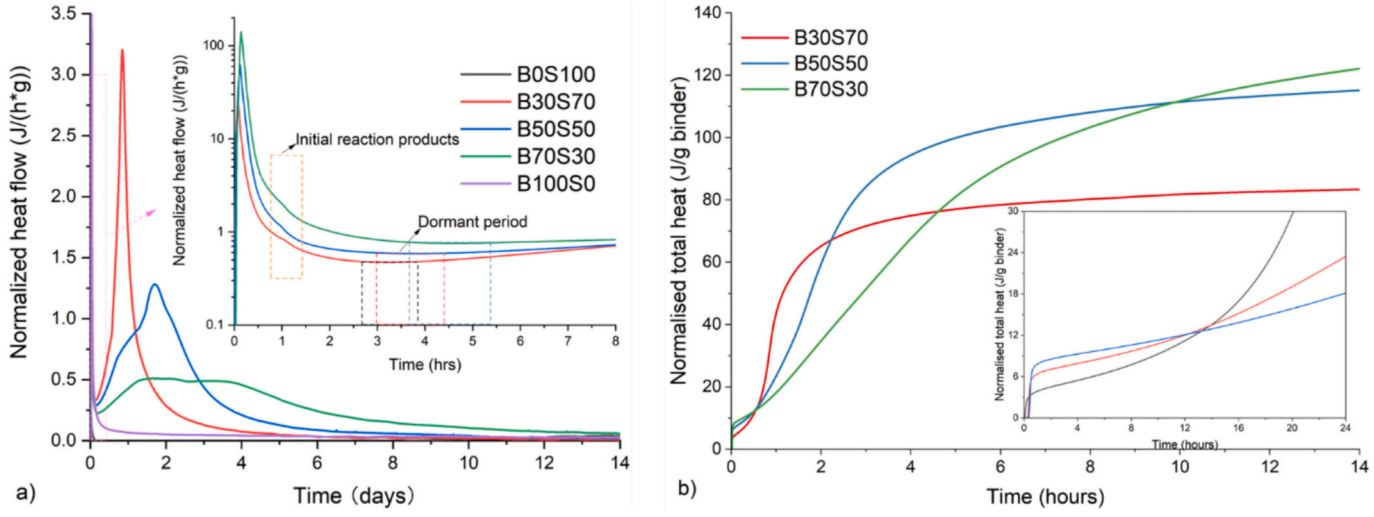

Fig. 3. Normalized heat flow (a) and cumulative heat of pastes (b).

and precipitation of hydrates at this stage. Afterwards, mixtures with lower WBFA contents tend to react more rapidly. For example, B30S70 maintains the highest cumulative heat up to approximately 2 days, while B50S50 exhibits the highest cumulative heat up to about 10 days, after which it is surpassed by B70S30. From long-term perspective, mixtures containing higher WBFA contents display a slower but more sustained increase in cumulative heat release over time. This behaviour reflects the complementary roles of the two components in the binary system. The potential roles of these two components will be further addressed in Section 4.1.

3.2. Pore solution chemistry

3.2.1. Ion concentrations

The ion concentrations in binary pastes at 1 day, 7 days, 14 days, and 28 days are presented in Fig. 4. The near charge balance between major cations and anions (Fig. 4 (a)) indicates an overall satisfactory analytical quality.

The concentration of [Ca] (Fig. 4 (b)) exhibits a marked decline from day 1 to day 7 in both B50S50 and B70S30, after which no significant changes occur. In contrast, B30S70 shows a slight increase in [Ca] concentration between 1 day and 7 days, followed by a minor decrease until 14 days and a marginal rise at 28 days. Overall, the concentration changes in [Ca] for B30S70 are comparatively small.

Since WBFA and BFS have similar calcium contents in their chemical compositions (about 40% wt%), the interpretation of variations in Ca concentrations is somewhat ambiguous. In contrast, the [Si] and [Al] in the pore solutions should mainly come from the dissolution of BFS. It is interesting to point out that the concentrations of [Si] and [Al] do not decrease proportionally with the decrease in BFS. The concentrations of [Si] in B50S50 and B70S30 are comparable at 1 day, and both are much lower than that in B30S70. The same trend is also seen for [Al]. Therefore, it may be inferred that the dissolution of BFS is delayed in samples with more WBFA. This also agrees with the results in isothermal calorimetry, where pastes with a larger amount of WBFA exhibit slower early reactions.

The alkalis (Na, K) in pore solutions mainly result from the dissolution of alkaline minerals, primarily originating from WBFA as indicated in Table 1. An intriguing observation can be seen in the concentrations of [K], where B70S30 contains a much higher amount of bulk potassium

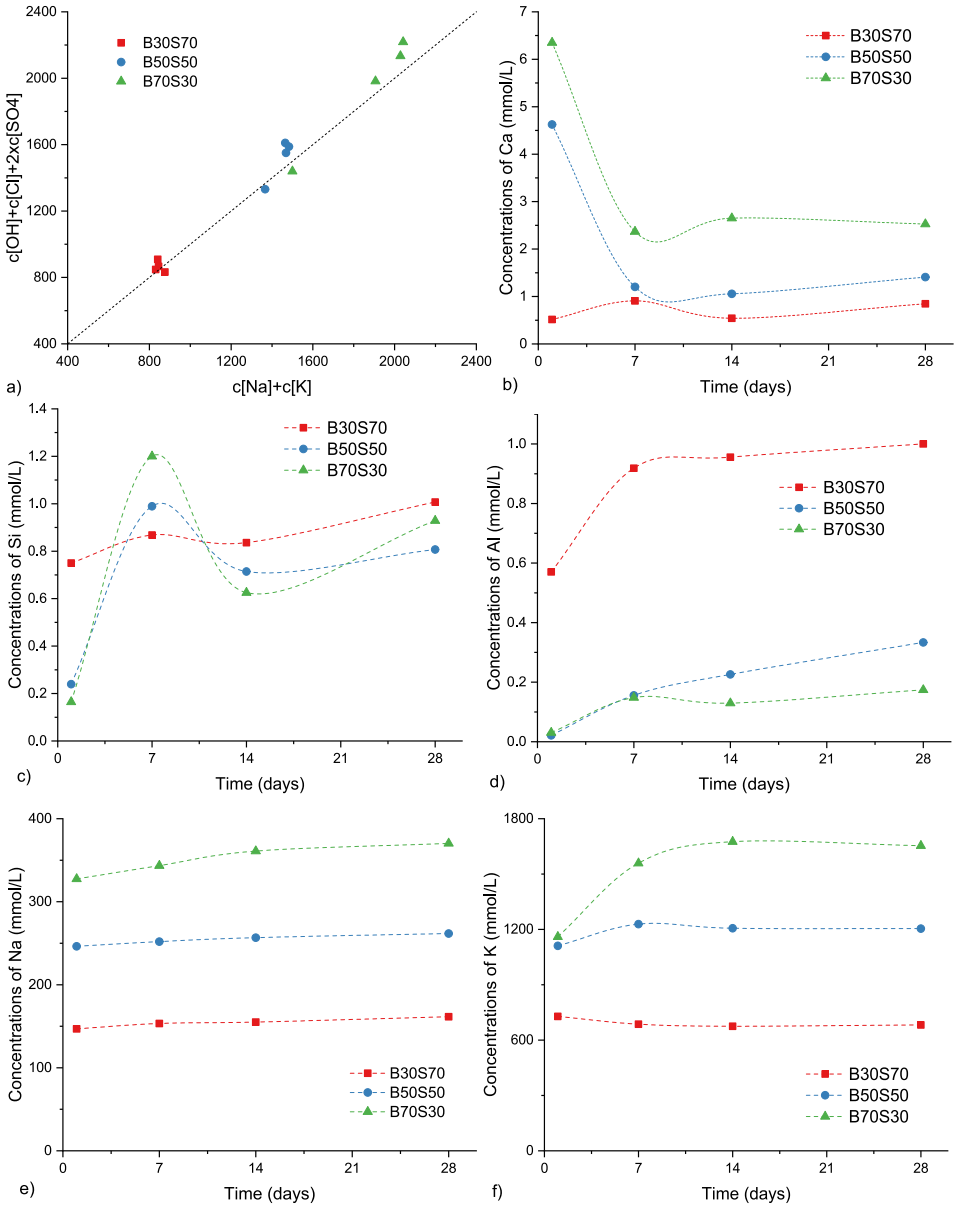

Fig. 4. Ion concentration in the pore solutions of pastes at 1 day, 7 days, 14 days, and 28 days.

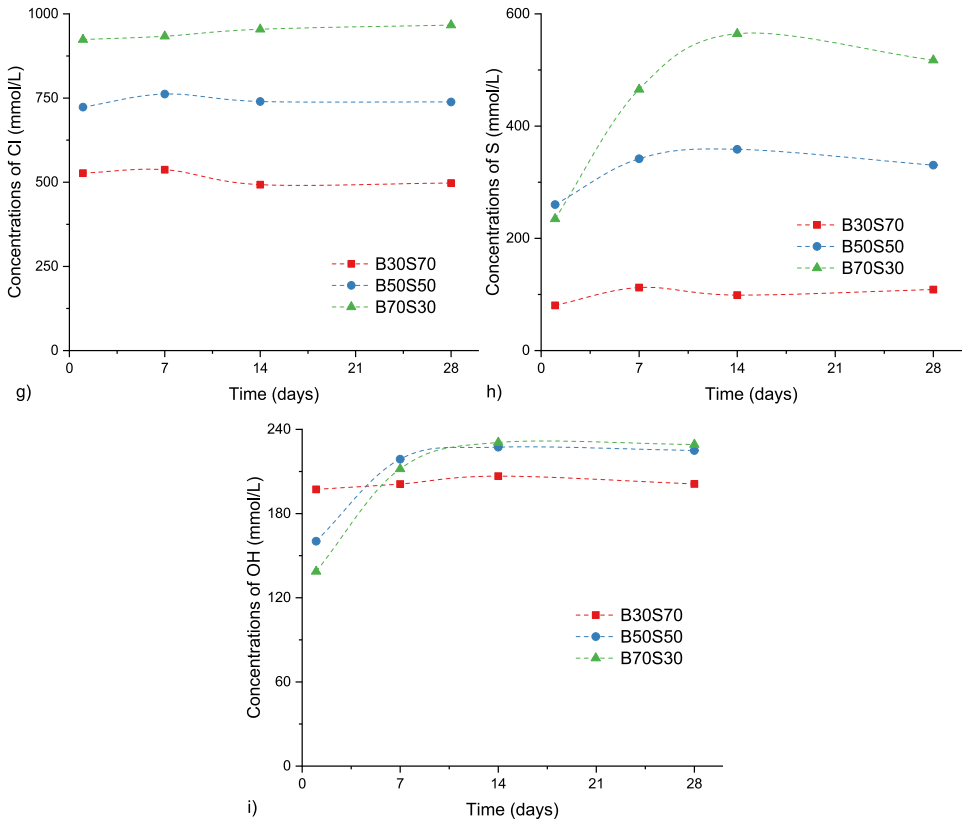

Fig. 4. (*continued*).

found with similar concentration of [K] to that of B50S50 at 1 day. Pastes with more WBFA show a more pronounced increment in the concentrations of [K] from 1 day to 7 days. This indicates that the initial dissolution of potassium salt in WBFA is to some extent hindered in pastes with a higher amount of WBFA.

For anions, chloride is primarily dissolved from sylvite (KCl) in WBFA, the main chloride-bearing phase with high solubility. Consequently, the concentrations of [Cl] are proportional to the amount of WBFA in the pastes. For B30S70 and B50S50, the concentrations of [Cl] show a slightly decrease over time, whereas B70S30 generally maintains a stable level. Given that the pore solution volume decrease as reaction progresses, this trend suggests the possible incorporation of chloride into newly formed chloride-bearing hydrates. The concentration of [S], on the other hand, exhibits an identical time-dependent trend to that of [K]. For instance, B70S30 contains a comparable concentration of both [S] and [K] to those in B50S50 at 1 day. The concentrations of these two elements show a similar increment with time until 28 days. Therefore, it is reasonable to infer that pastes with more WBFA might exhibit a delayed initial dissolution of minerals containing these two elements, such as aphthitalite and syngenite. This behaviour may be associated with the formation of initial hydration products during the first few hours, which could partially hinder further dissolution of WBFA slow down the reaction. Further discussions will be addressed in Section 4.1.1.

The concentration of [OH] is shown in Fig. 4 (i). Despite WBFA is the main alkaline resource in the pastes, it is surprising to find that samples with a higher WBFA/BFS ratio have a lower concentration of [OH] at 1 day. The concentrations of [OH] in B50S50 and B70S30 increase rapidly from 1 day to 7 days, then remains almost constant until 28 days. In contrast, the concentration of [OH] in B30S70 is rather stable from 1 day to 28 days. Based on the development of alkalinity of pore solutions, together with the concentrations of [K] and [S] from WBFA, and [Si] and [Al] from BFS, the evidence further supports that the initial dissolution of both WBFA and BFS is restrained in pastes with a higher proportion of WBFA. Still, it is important to note that this does not indicate that WBFA only presents a side effect in the hydration of binary pastes. With the increment of WBFA, the significant increase in alkalinity in later hydration promotes the dissolution of aluminosilicates from BFS, which can be convinced by the increased concentrations of [Al] and [Si] at later hydration.

3.2.2. *Effective saturation indices (ESI)*

Based on the compositions of pore solutions, it is possible to predict the potential hydrates using thermodynamics. To conduct this analysis, a Gibbs Energy Minimization Software (GEMs) [35,36] with the CEMDATA18 database [37] was applied, using the ion concentrations of the pore solutions reported in Section 3.2.1 as input. This enables the calculation of ESI for specific hydrates, providing an indication of the possible hydrates that may form. A positive value of ESI indicates the potential precipitation of a specific phase, while a negative value means the phase is undersaturated and therefore cannot be generated. An error and uncertainty range of ± 0.20 is recommended considering the uncertainties of the solubility products [38]. Based on the ions available, the ESI of C-A-S-H gels, ettringite, portlandite, and the chloride-bearing hydrate Friedel's salt were calculated, enabling an initial estimate of possible hydrates and allowing exploration of the reasons for the evolution of ion concentrations over time.

As shown in Fig. 5, C-(A)-S-H gels and ettringite are the most probable hydrates to be formed in the binary pastes, which are also commonly reported as the main hydrates in cement [39,40]. The chloride ion is assumed to be encapsulated within the hydrates due to the general decrease in its concentrations over time. Hence, the ESI of the two commonly formed chloride-containing hydrates in cementitious materials, namely Kuzel's salt and Friedel's salt, were calculated. Although some negative values were obtained in mixtures with a low WBFA/BFS ratio (especially for Friedel's salt), it is important to note that

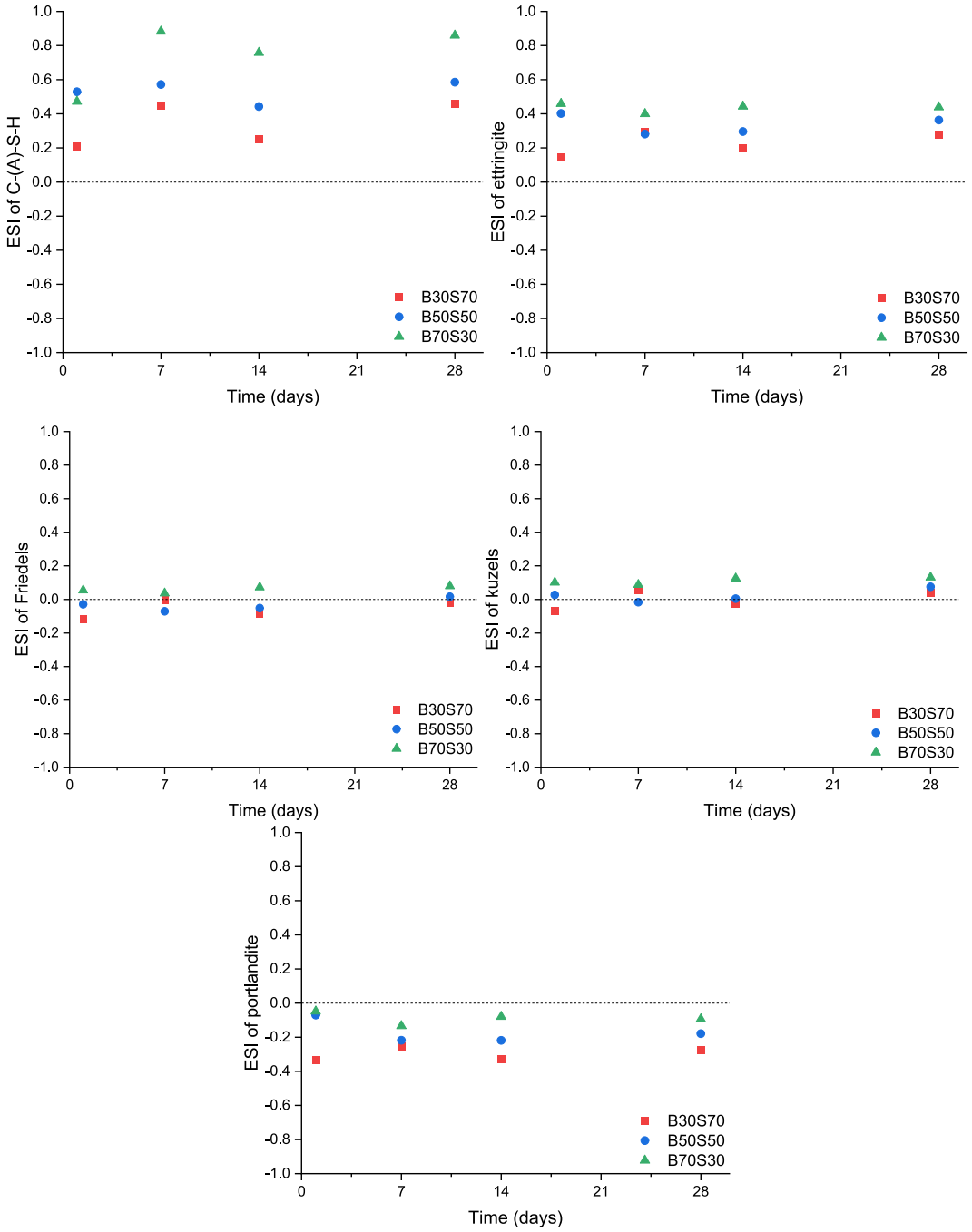

Fig. 5. ESI of phases of interest.

these values are still above the uncertainty bound (-0.2). Therefore, it remains thermodynamically feasible for the precipitation of these two phases to occur. For portlandite, its negative ESI is consistently observed in all mixtures from 1 day to 28 days. Since portlandite is one of the minerals present in WBFA (5.56% wt.), its continuous consumption can be expected during the hydration of the binary pastes. A detailed characterization of the reaction products using XRD is provided in the following sections to confirm the hydrates that actually form.

3.3. Solid phases

3.3.1. XRD analysis

The XRD patterns of binary pastes at 7 days and 60 days are plotted in Fig. 6. Generally, the phase compositions of the three mixtures are consistent. The primary crystalline phases observed include ettringite, Friedel's salt, portlandite, quartz, and calcite in all mixtures, irrespective of the curing ages.

Quartz and calcite are two stable phases originating from WBFA. Ettringite is identified as one of the main crystalline hydration products, with strong diffraction peaks observed in all binary pastes. This finding is consistent with the ESI calculations, which predict the precipitation of ettringite during the hydration of the binary systems. The intensity of portlandite diffraction peaks decreases noticeably from 7 to 60 days in all mixtures, indicating its progressive consumption via reaction with BFS, which aligns closely with the ESI results. Friedel's salt is the only chloride-bearing phase detected in the pastes, while no Kuzel's salt is observed, despite its potential formation suggested by the ESI calculations. This absence can be attributed to the highly chloride-rich

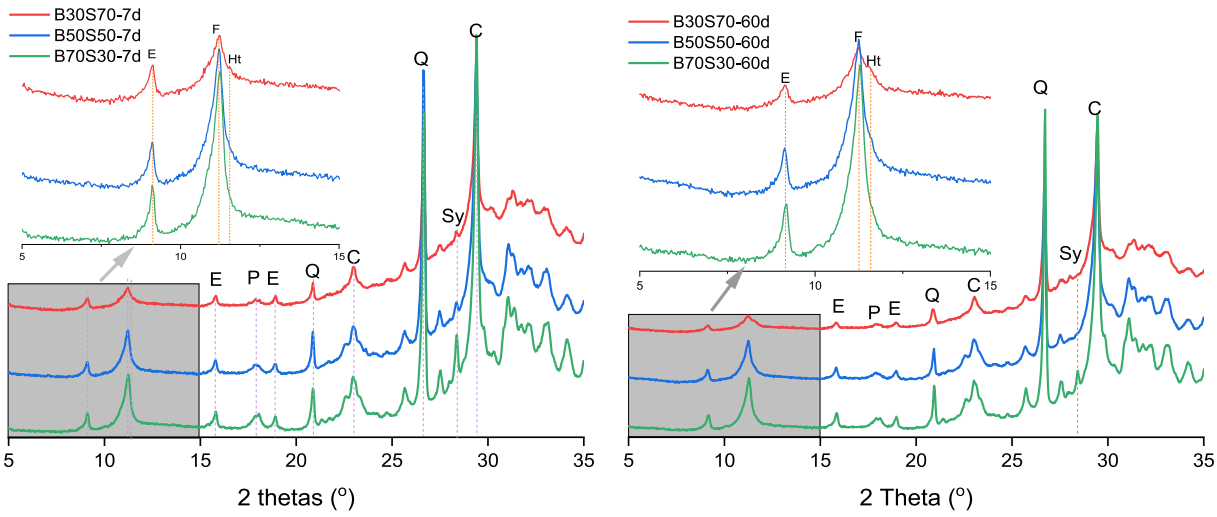

Fig. 6. XRD patterns of binary pastes at 7 days (left) and 60 days (right) (E: ettringite, F: Friedel's salt, Ht: hydrotalcite, P: portlandite, Q: quartz, C: calcite, Sy: sylvite).

environment, where Kuzel's salt tends to act as a transient intermediate, and Friedel's salt forms the more stable end-product [41–43].

A weak hydrotalcite diffraction peak is detected in B30S70 at 7 days. The intensity of the hydrotalcite diffraction peak becomes notably stronger in B30S70 at 60 days, and a similar but weaker peak is also observable in B50S50 at 60 days. It is noteworthy that the strong diffraction peak of Friedel's salt can overlap with that of hydrotalcite, complicating phase differentiation. Since the concentration of Mg is too low to exceed the detection limit in the pore solution, the ESI of hydrotalcite cannot be calculated.

Besides crystalline hydrates, the other main hydrate, C-(A)-S-H gels can only produce a broad diffraction hump in the XRD pattern at around 29° due to the semi-crystalline nature [44]. However, with the presence of unreacted BFS and calcite from WBFA, the diffraction hump of C-(A)-S-H might be obscured. Therefore, FTIR is further applied to identify the chemical bonds reflecting the existence of C-(A)-S-H gel phases.

3.3.2. FTIR analysis

The FTIR spectra of pastes at 7 days and 60 days are plotted in Fig. 7, compared with those of the raw materials, with the adsorption bands indicated. It can be seen that BFS shows the main adsorption band at 899 cm^{-1}, and could be attributed to the vibration of Si-O-T, where T represents Si or Al [45]; comparatively, WBFA shows the main bands at 1420 cm^{-1} and 875 cm^{-1}, associated with carbonate minerals, and at 1105 cm^{-1}, which should be attributed to the reactive Si—O bands.

In the binary pastes, the main bands of all samples are located at approximately 950 cm^{-1}, which is associated with the stretching vibration of Si—O bonds (Q2). This is a typical signal for the presence of C-(A)-S-H gels as previously reported in the literatures [46,47]. The shift of the main IR band relative to the raw materials therefore confirms that reactions occur between the two materials, leading to the formation of C-(A)-S-H as the main reaction product in the binary pastes. Other Si—O bonds that relate to C-(A)-S-H gels with lower intensities occur at 815 cm^{-1} and 1037 cm^{-1}, and should be assigned to Q1 and Q2 silicate species, respectively [48]. These bands become more pronounced over time as the fact of the continuous formation of C-(A)-S-H gels with the increasing of curing age.

The band at 3640 cm^{-1} is the O—H stretching vibration and should be assigned to portlandite [46]. The intensity of the portlandite band increases in samples with higher WBFA/BFS ratios and decreases as hydration progresses. This is in line with the ESI calculations indicating the depletion and consumption of portlandite during the hydration process. Bands at 3400 and 1640 cm^{-1} can be attributed to the asymmetric stretching and bending of O—H, respectively [49]. These bands exist in the hydration products as chemically bonded water. Bands at 796 cm^{-1} should be attributed to Al-OH, and are assigned to ettringite

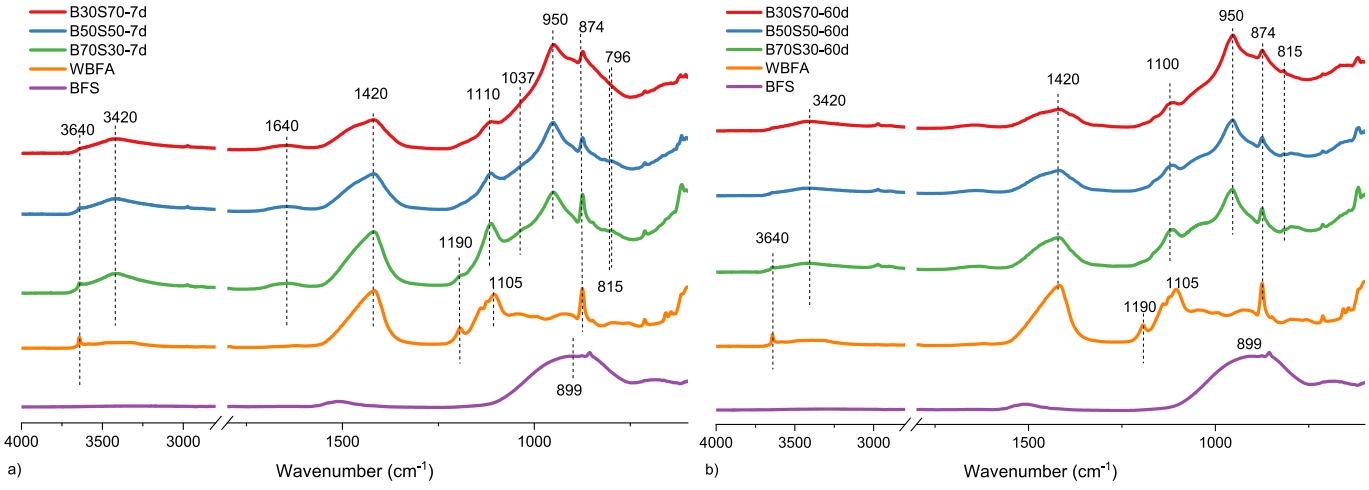

Fig. 7. FTIR spectra of WBFA-BFS pastes at 7 days and 60 days.

[50]. These results are in line with ESI and XRD results in general, confirming the formation of C-(A)-S-H gels, ettringite, and progressive depletion of portlandite.

3.3.3. TG/DTG analysis

The TG and DTG curves of the binary pastes are shown in Fig. 8. The main DTG peak is located at approximately 110 °C. Based on the hydrate components, it can be deduced that this peak is attributed to the decomposition of C-(A)-S-H gel [28] and ettringite [51]. These two phases are known to exhibit an overlapped decomposition temperature range [52]. The double-layered hydrates (Friedel's salt and hydrotalcite) have been reported to exhibit doublet decomposition peaks in DTG curves with similar decomposition temperatures [41]. They are characterized by the first shoulder occurring at approximately 170 °C, followed by a second peak around 320 °C. Additionally, a small DTG peak between 400 and 500 °C is associated with the decomposition of portlandite. Decarbonation occurs predominantly above 600 °C, mainly due to the decomposition of calcite and carbonate-bearing minerals originating from WBFA.

The dehydration and dehydroxylation of hydrates result in mass loss, which is directly proportional to the amount of hydrates. Fig. 9 shows the amount of bound water in different mixtures at 7 days, 28 days, and 60 days. The bound water content is calculated from the mass loss within the temperature range of 40-550 °C [28]. The increase in mass loss over time suggests continued hydration of pastes. Since the compositions of hydrates differ among pastes with varying WBFA/BFS ratios, it is not meaningful to directly compare the absolute values of mass loss between different mixtures to index the overall reaction degree of the binder. However, the changes in mass loss with time for an individual mixture can be indicative of its internal reaction development. Overall, the rate of bound water increase follows the trend B30S70 < B50S50 < B70S30

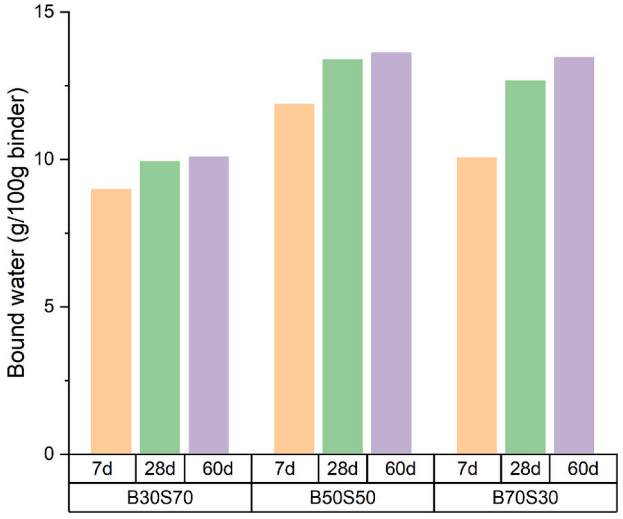

Fig. 9. Evolution of bound water in binary pastes.

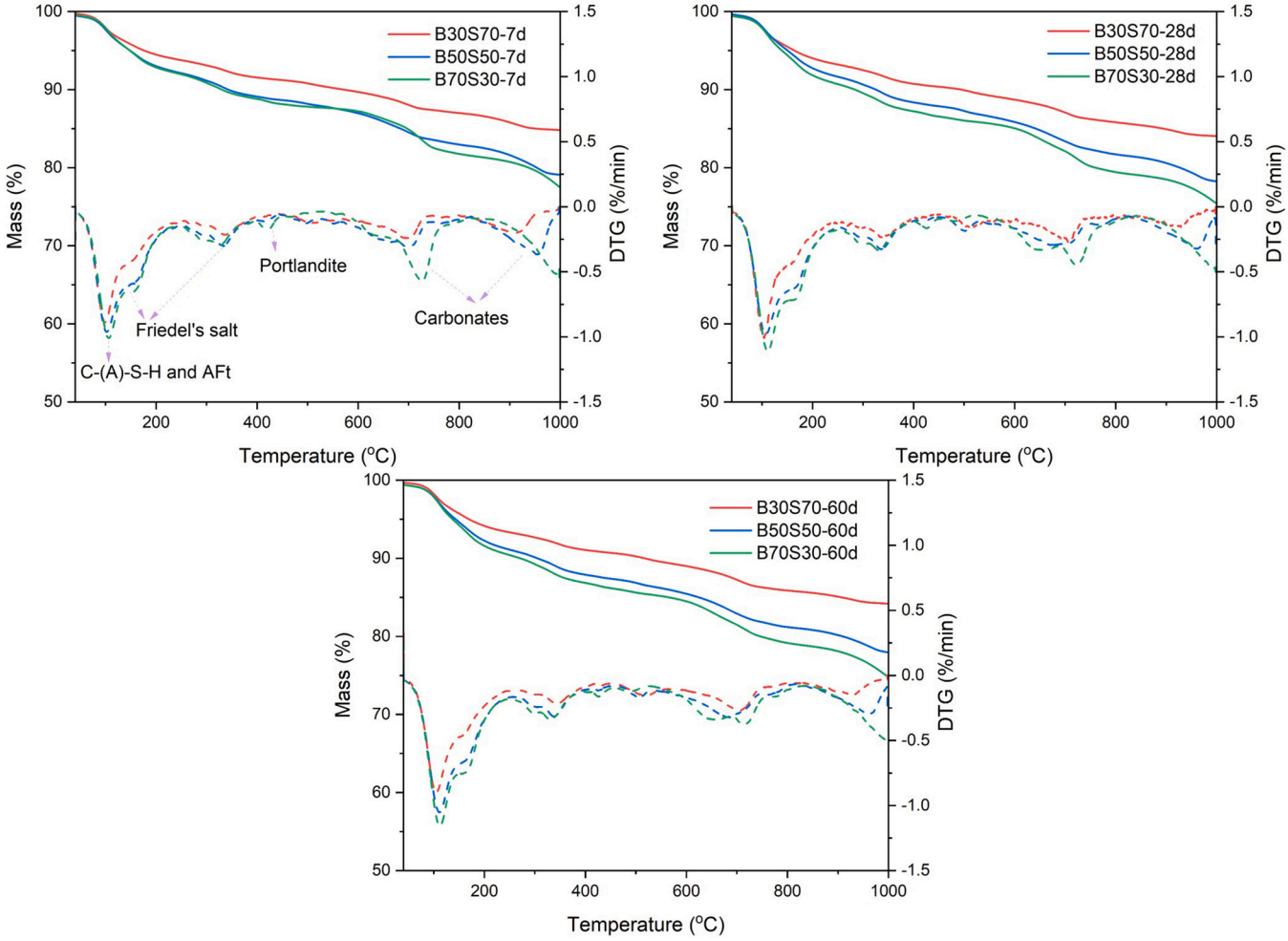

Fig. 8. TG/DTG curves of WBFA-BFS pastes at 7 days, 28 days, and 60 days (Solid lines represent the TG results and dashed lines represent DTG results).

from 7 days to 60 days. Mixtures with higher WBFA/BFS ratios have a faster development of bound water, suggesting more precipitation of hydrates. This result also agrees with findings from previous sections that larger WBFA/BFS ratios progressively promote the hydration of binary pastes at a later stage.

3.4. Microstructure development

3.4.1. Pore volume and size

The MIP results for binary pastes are presented in Fig. 10. The binary pastes show a highly porous microstructure. The total intrusion porosity of the pastes ranges between 30 and 45%, which is generally higher than that reported for Portland cement pastes with a similar water-to-binder ratio [40,53].

The total intrusion porosity of the pastes decreases with time, which can be attributed to continuous hydrate precipitation that fills pore spaces and densifies the microstructure. Notably, regardless of curing age, B50S50 exhibits the lowest porosity among the mixtures. Moreover, an interesting observation is the more pronounced reduction in intrusion porosity from 7 days to 60 days in B50S50 and B70S30 compared to B30S70. This phenomenon can be associated with the reaction rate from a long-term perspective. As indicated by the development of bound water, mixtures with a larger WBFA/BFS tend to show a more pronounced bound water increase, facilitating the generation of more hydrates and subsequently reducing porosity.

The pore size distribution of pastes were divided into five categories, namely gel pores (<10 nm), micro capillary pores (10–50 nm), medium capillary pores (50–100 nm), large capillary pores (100–1000 nm), and air voids (>1000 nm) as shown in Fig. 4.10(a) [53–55]. Capillary pores are the dominant pore type, accounting for >75% of the intrusion pore volumes regardless of mixture composition and ages. It is evident that pastes with higher WBFA/BFS ratios exhibit a higher volume fraction of large and medium capillary pores at 7 days, which can be interpreted from the aspect of the initial particle packing. As WBFA particles have a larger size compared to BFS particles, an increase in WBFA content will results in an increase in larger particles packing to form large pores, which are not adequately filled with insufficient numbers of small particles.

The refinement of pore structures through hydrate formation that fills pore spaces leads to an increase in the proportions of micro capillary pores. A noticeable reduction in pore size is indicated by the shift of the differential pore size distribution curves (Fig. 10 b), c), and d)) towards lower values over time. The critical pore size, which corresponds to the point of steepest increase in pore volume and is closely related to the

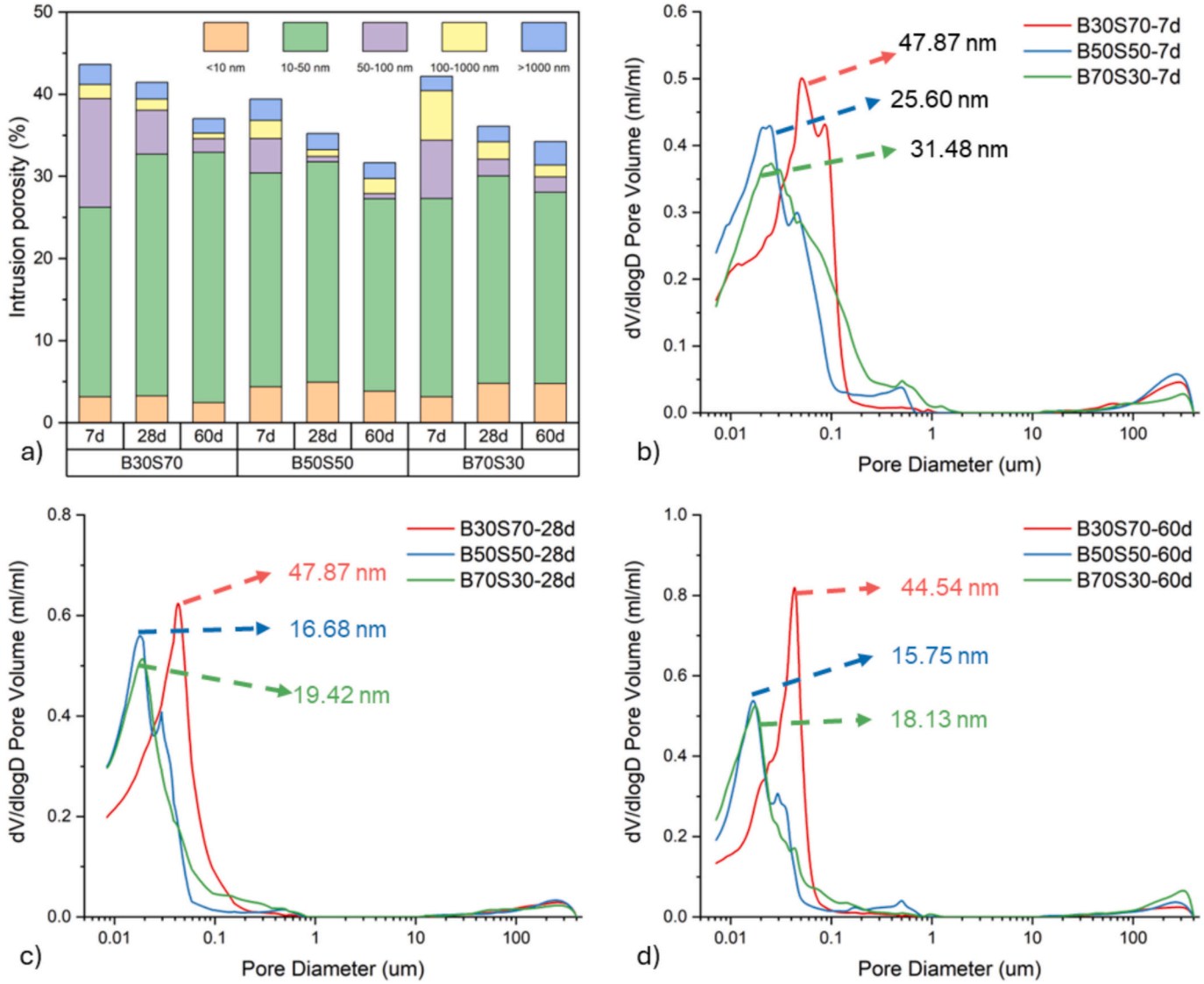

Fig. 10. Pore proportions (a) and differential pore size distribution (b, c, d) of binary pastes.

transport properties and strength of the pastes, was used as an indicator to compare the pore structures among the three groups. The critical pore size for each mixture is marked accordingly in these figures. B30S70 shows the largest critical pore size at all ages, and its reduction in size was less pronounced compared to the other two groups. Larger WBFA/BFS ratios promote greater hydrate precipitation, especially at later hydration, leading to a more significant effect on the pore refinement.

3.4.2. Microscopy analysis

Fig. 11 displays the BSE images of pastes at 7 and 60 days with a magnification of 2000×. Owing to the variation in the average atomic number among different phases, it is feasible to identify unreacted BFS and WBFA particles from their grey levels. Anhydrous BFS particles are represented by bright areas. WBFA particles show both angular and spherical geometries represented by a broad range of grayscale values ranging from relatively dark regions (mainly quartz) to bright particles, indicating the heterogeneous nature of WBFA. The black region represents epoxy-immobilized pores. The hydrates appear as dark grey, with a grey level between those of the pores and anhydrous particles. From the BSE images, it can be observed that anhydrous particles adhere to the hydration products and form the microstructure of the pastes. In general, a porous and relatively loose microstructure is observed in all pastes compared with Portland cement matrices [56–58].

To further analyse the influence of mixture proportion on the chemical composition of reaction products, the EDS hypermaps of samples at 60 days were segmented into three categories, namely, pores, anhydrous particles, and hydrates, using the Edxia method [59]. The corresponding phase segmentations are presented in Fig. A2. Based on elemental ratio constraints proposed in [59], further sub-phase segmentation was applied within the hydrate domain, as plotted in Fig. 12 (a)-(c). The hydrate assemblage is dominated by intermixed C–(A)–S–H gels, ettringite, Friedel's salt, and hydrotalcite. In the EDS scatter plots, the point density of each hydrate phase reflects a semi-quantitative indication of their abundance in hydrate phases. With increasing WBFA content, the scatter intensity associated with ettringite and Friedel's salt become progressively more pronounced, implying that WBFA facilitates the generation of these two phases. It should be noted that although only a limited scatter points are observed in the ettringite and Friedel's salt domains for B30S70, XRD analysis confirms the presence of these phases, indicating that their weak representation in the EDS plots reflects their low abundance rather than their absence. In addition, although C–(A)–S–H remains the dominant hydrate phase across all mixtures, an increase in WBFA content leads to a systematic decrease of Si/Ca ratio in C-(A)-S-H gels as shown in Fig. 12(d), which can be attributed to the higher calcium availability combined with the limited contribution of reactive aluminosilicate species from WBFA during hydration.

3.5. Compressive strength

Fig. 13 shows the compressive strength of binary pastes, with their strength improvement ratios relative to the 7-day strength marked accordingly. Due to the high porosity of these pastes, their compressive strength is relatively low compared to Portland cement pastes or waterglass-activated slag [60,61]. However, it is comparable to sodium salt and lime-activated slag [62,63]. In particular, B30S70 exhibits a

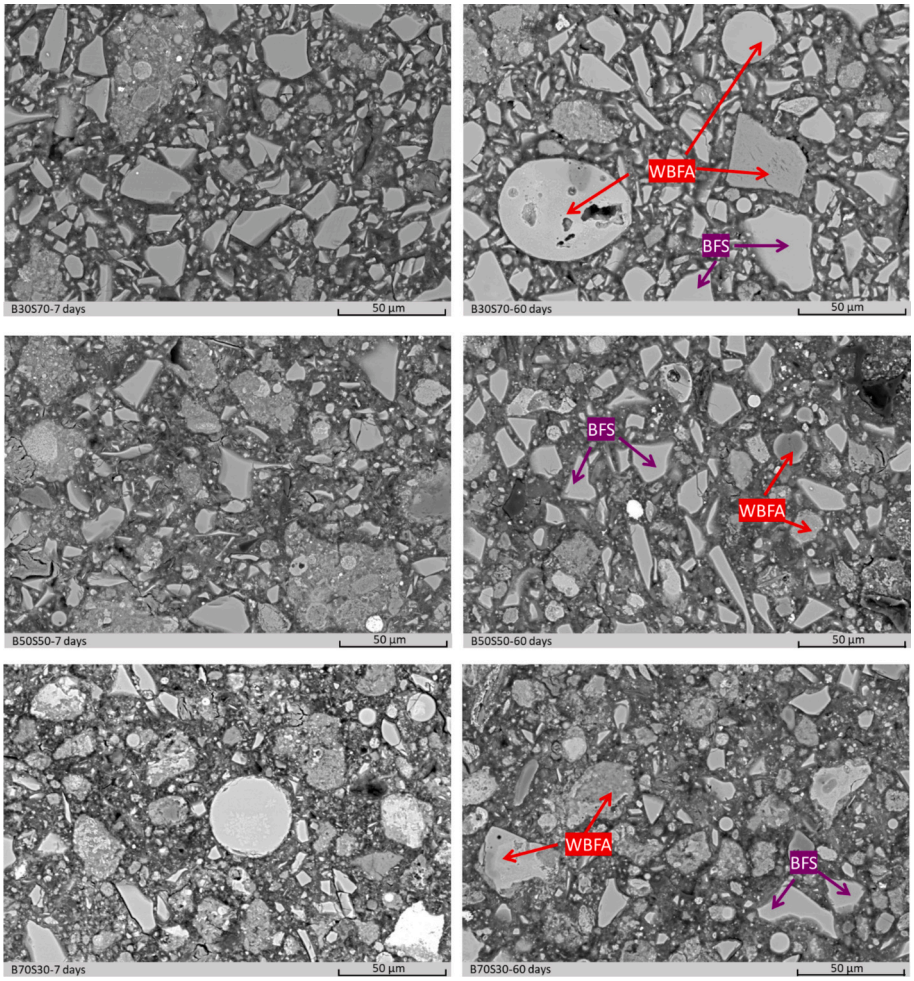

Fig. 11. BSE images of binary pastes.

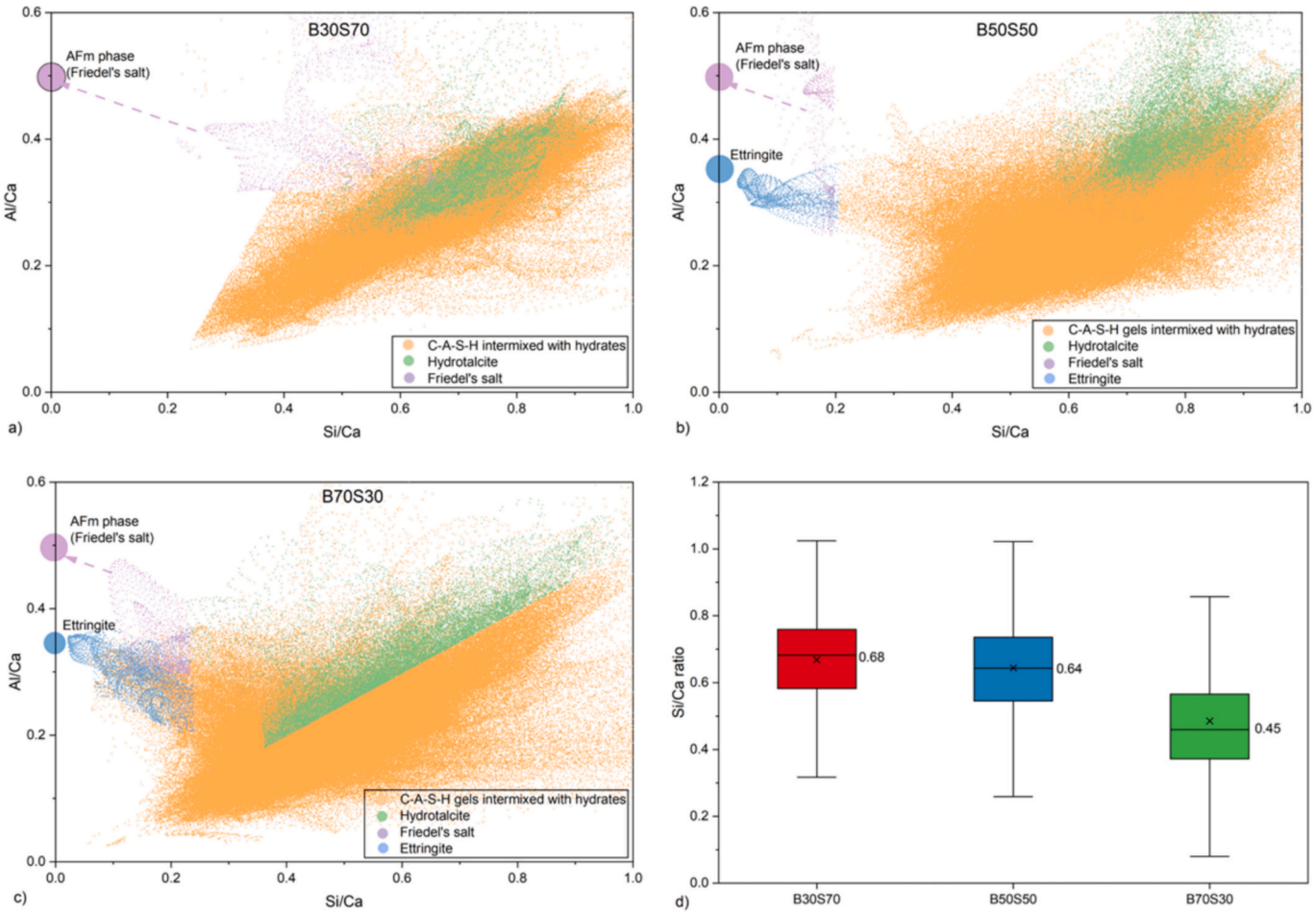

Fig. 12. EDS scatter plots of hydration products at 60 days (a:B30S70, b:B50S50, c: B70S30; Yellow markers represent C-(A)-S-H gels intermixed with other hydrates; purple markers indicate AFm phases; blue markers represent ettringite; and green markers denote hydrotalcite-like phases; d: box-plot of scatter of C-(A)-S-H regarding Si/Ca ratio). (For interpretation of the references to colour in this figure legend, the reader is referred to the web version of this article.)

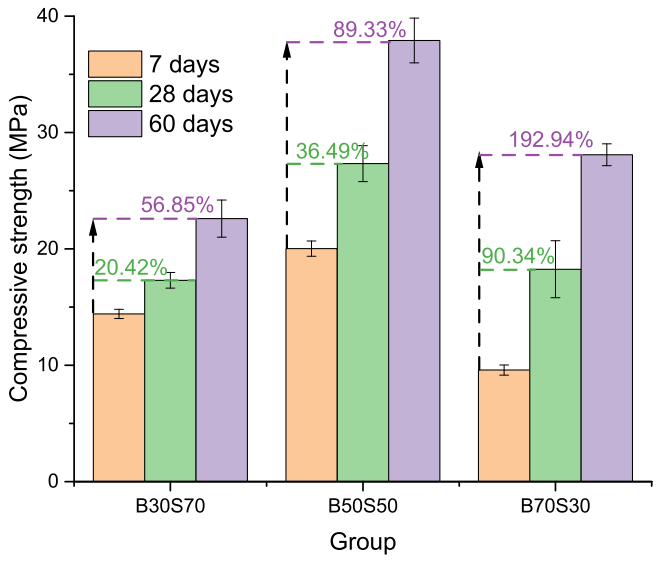

Fig. 13. Compressive strength of binary pastes.

compressive strength of 14.41 MPa at 7 days and shows the smallest strength improvement, reaching 22.61 MPa at 60 days. In contrast, B70S30 demonstrates the most pronounced strength development, increasing from 9.59 MPa at 7 days to 28.09 MPa at 60 days. Among the mixtures, B50S50 presents the highest compressive strength throughout all curing stages, increasing from 20.02 MPa at 7 days to 37.91 MPa at 60 days.

As discussed in the previous sections, B30S70 exhibits a faster early reaction, as indicated by calorimetry; however, its later-stage reaction becomes limited, evidenced by a less pronounced increase in bound water content and a relatively limited degree of microstructural densification, which explains its slow strength evolution with time. In contrast, B70S30 shows a slower early reaction but sustains hydration over longer curing periods, leading to continuous microstructural refinement and significant strength gain at later ages. Among the mixtures, B50S50 exhibits the highest bound water content, indicating the formation of hydration products in greater quantities. Meanwhile, it demonstrates a clear pore refinement process characterized by a reduced critical pore size and the lowest total porosity, which ultimately results in the highest compressive strength among the three mixtures.

4. Discussions

4.1. Reaction kinetics of binary pastes

4.1.1. General discussions

Isothermal calorimetry (Fig. 2) shows that within the first 10 h the heat flow and cumulative heat release are higher in mixtures containing larger amounts of WBFA, indicating more intensive dissolution and initial precipitation of hydrates. Specifically, the cumulative heat within

the first 10 h follows the order B70S30 > B50S50 > B30S70. Afterwards, mixtures with lower WBFA content exhibit a more intensive reaction, as evidenced by B30S70 showing the highest cumulative heat up to approximately 2 days. With extended curing, mixtures containing higher WBFA contents show more intensive reaction. Thus, the cumulative heat of B50S50 gradually surpasses that of B30S70 after 2 days, while B70S30 exhibits the highest cumulative heat after approximately 10 days. The role of WBFA in sustaining long-term hydration is further supported by the most significant increase in bound water content and the pronounced pore refinement observed in B70S30.

From the pore solution perspective, although WBFA acts as the primary alkali source in the system, the concentration of [OH] at 1 day is lowest in B70S30 and highest in B30S70. Meanwhile, the concentration of [K] does not scale proportionally with the WBFA content at 1 day but becomes more proportional at 7 days and thereafter. This indicates that at 1 day, the dissolution of WBFA is initially hindered, followed by a slower and more sustained release of alkalis at later stages. Based on these observations, one possible reason for the restrained dissolution of WBFA could be attributed to the formation of initial hydration products during the early dissolution stage. These products, generated in larger quantities in mixtures with higher WBFA contents, as indicated by the higher heat flow and cumulative heat within first 10 h, may partially inhibit the further dissolution of WBFA. Nevertheless, this restrained dissolution mainly affects early hydration, while the dissolution of WBFA continues with time and plays a more pronounced role during the later stages of hydration. The kinetics of the binary reactions are further discussed in the following sections.

4.1.2. Reaction degrees of BFS

The hydration degrees of BFS were calculated based on the BSE-EDS mapping described in Appendix A (associated with Fig. A1), and the results are presented in Fig. 14. Comparable reaction degrees of BFS were observed at 7 days for all mixtures. However, a high WBFA/BFS ratio is found to significantly promotes BFS hydration in the long term. For instance, the reaction degrees of BFS increase from 31.41% to 42.22% from 7 days to 60 days in B70S30. In contrast, for B30S70, the increase is much smaller, from 25.68% to 28.78% over the same period. This result directly confirms the discussions in previous sections that larger WBFA/BFS ratios facilitate the long-term hydration of BFS.

Based on the reaction degrees of BFS, the reacted amount of BFS in the binders was calculated and the results are listed in Table 3. It is noted that although the reaction degrees of BFS in B70S30 reach up to about 40%, the absolute amount of reacted BFS is still relatively low, especially compared to the amount in B30S70. To comprehensively illustrate the reaction kinetics of the binary pastes, the contribution of WBFA in the reaction is of great interest.

Table 3
Amount of reacted BFS in pastes (g/100 g binder).

	B30S70	B50S50	B70S30
7 days	17.97	15.81	9.42
60 days	18.74	19.38	12.67

4.1.3. Reaction contribution by WBFA

Owing to the complexity of WBFA, it is difficult to determine the reaction degree of WBFA using the available experimental techniques. Still, one approach to investigate the contribution of WBFA to the reaction is to consider the perspective of reaction enthalpy, which is largely dependent on the reaction degree of binders.

The exponential equation presented in Eq. 1 has been widely reported to be one of the best mathematical functions for fitting the reaction enthalpy of cementitious materials [64],

$$Q(t) = Q \times \exp\left(-\frac{\tau}{t}\right)^{\beta} \quad (1)$$

where Q(t) is the cumulative heat of binder (J/g) released at time t (hours), Q is the heat released at the final reaction degree, τ is the hydration time parameter, β is the shape parameter.

The fitted normalized total heat, as shown in Fig. 15 agrees well with the experimental data. As the reaction degree of BFS has been determined by image analysis, the enthalpy of BFS at 7 days and 60 days can be calculated according to Eq. 2,

$$Q_i(t) = Q_{max,i} \times \alpha_i(t) \quad (2)$$

where $Q_i(t)$ is the heat released by the reactive component I (BFS) at time t; $Q_{uax,\,i}$ is the maximum enthalpy of the component (corresponding to 100% of reaction); $\alpha_i(t)$ is the reaction degree of the reactive component at time t.

To calculate the heat release from BFS, it is essential to know the maximum enthalpy for the BFS reaction ($Q_{max,\,slag}$). According to the literature [65,66], the enthalpy of BFS is approximately 400 J/g. Although this is an estimation of $Q_{max,\,slag}$, the results remain informative for further analysis of the contribution of WBFA. By subtracting the heat contribution from BFS, the released heat contributed by WBFA can be isolated. The reaction contributions of BFS and WBFA in terms of

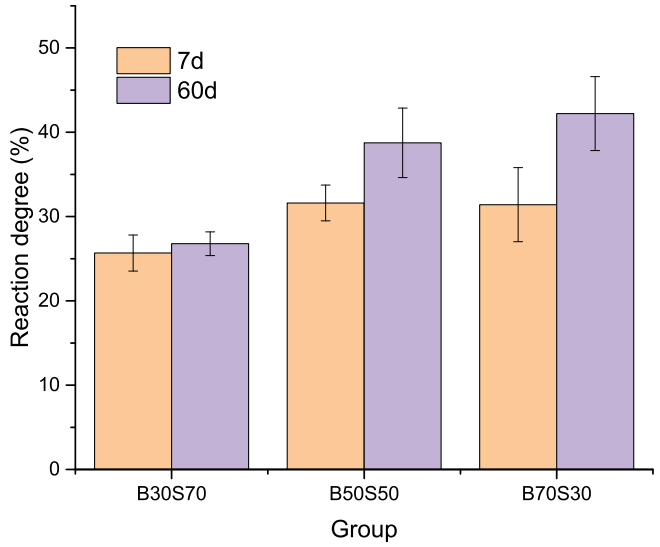

Fig. 14. Hydration degrees of BFS determined by BSE-EDS mapping analysis.

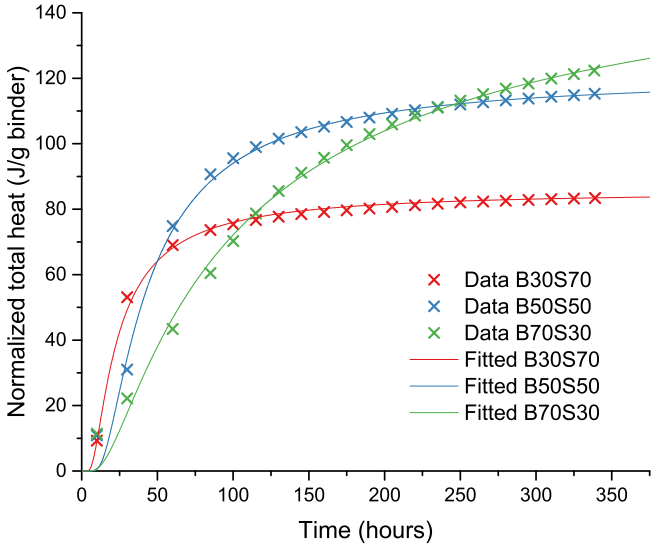

Fig. 15. Calculated normalized total heat of binary pastes.

heat release are shown in Fig. 16. Besides supplying alkalis and sulphate that promote the reaction of BFS, WBFA itself can also participate in the reaction process through the dissolution of its reactive amorphous phases in the binary pastes. Consequently, WBFA contributes to the overall heat release of the system, particularly in mixtures containing a higher proportion of WBFA.

4.1.4. Reaction kinetics

Based on the released heat of BFS and WBFA at 7 days and 60 days, it is, however, challenging to present a time-dependent reaction kinetics model for each component, unless at least one parameter (Q, τ, β) in the exponential equation is defined. Besides the exponential equation, another empirical equation, Knudsen's equation (shown in Eq. 3) [67,68], has also been widely used for the determination of the parameter Q in cementitious materials:

$$\frac{1}{Q(t)} = \frac{1}{Q}\left(1 + \frac{t_{50}}{t - t_0}\right) \tag{3}$$

where Q(t) is the cumulative total heat of binder (J/g) at time t, t_0 is the end of the induction period, t_{50} is the time needed to reach 50% reaction degree for cementitious materials.

This equation implies a linear relationship between 1/Q(t) and 1/(t-t0). It has been confirmed that this equation accurately determines Q when a longer measuring time (>3 days) is available [67]. To validate the feasibility of Knudsen's equation for the binary pastes, a comparison of the fitted Q obtained from both the exponential equation and Knudsen's equation has been conducted, with the results presented in Table A2. The Q values show good agreement between these two methods. Based on the released heat from WBFA and BFS at 7 days and 60 days in Fig. 16, therefore, it is applicable to apply Knudsen's equation to calculate the value of Q of WBFA and BFS individually. The calculated Q of WBFA and BFS in different mixtures are presented in Table A3.

To further establish the reaction kinetics of these two components, their reaction degrees should be calculated. It is important to note that the Q is different from the Q_{max}. Q_{max} is assumed to be the enthalpy corresponding to 100% reaction, while Q is the eventual heat that can be released when the component reaches its ultimate (<100%) reaction extent. Therefore, it is possible to calculate the maximum reaction degrees of each component using Eq. 4, and to further establish the time-dependent reaction equation using Eq. 5:

$$\alpha_{ut,i} = \frac{Q_i}{Q_{max,i} \times W_i} \times 100\% \tag{4}$$

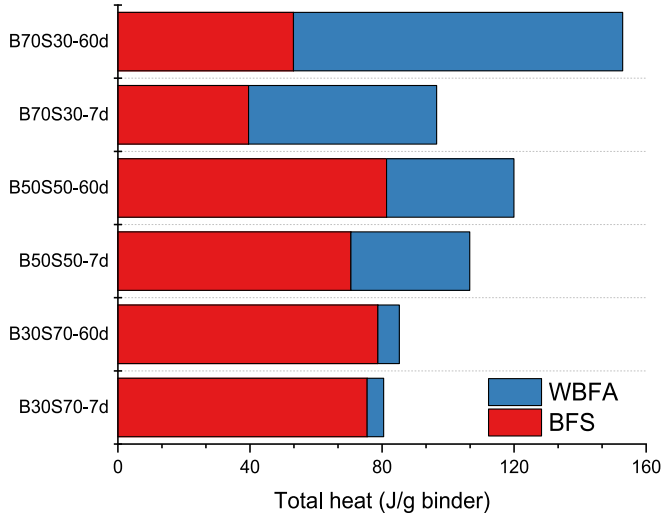

Fig. 16. Calculated total heat of binder contributed from BFS and WBFA.

$$\alpha(t) = \alpha_{ut,i} \times \exp\left(-\frac{\tau}{t}\right)^{\beta} \tag{5}$$

where W_i is the weight ratio (wt%) of one component in the binder.

With the current data, it is possible to establish the reaction kinetics equation for BFS. However, to also establish the reaction kinetics equation for WBFA, the Q_{max} of WBFA is needed. For now, only limited information is available on the Q_{max} of WBFA. One possible approach is to refer to the Q_{max} of high calcium coal fly ash. Schindler et al. [64] found that for high calcium coal fly ash, Q_{max} can be approximated by Eq. 6:

$$Q_{max,\ FA} = 1800 \times P_{FA,CaO} \tag{6}$$

where $P_{FA,CaO}$ is the weight proportion (wt%) of calcium oxide in fly ash.

It is essential to note that the calcium oxide in Eq. 6 mainly refers to the reactive calcium content. While in WBFA, it is assumed that this is mainly contributed by the reactive calcium oxide in the amorphous phases. The remaining calcium salts mainly influence the heat release only during the initial stage of hydration, which has already excluded when fitting the cumulative curves. Based on our previous research [12], the amorphous calcium oxide content in WBFA is 20.86%, thus the $Q_{max,\ FA}$ is 375.48 J/g.

Following the approach, the reaction kinetics of BFS and amorphous phase of WBFA in the binary mixtures were established, as shown in Fig. 17.

It is important to note that for the reaction degree of WBFA, several assumptions were made in the calculation. Since the $Q_{max,\ FA}$ is obtained by considering the amorphous phase in WBFA, the reaction degree of WBFA in Fig. 17 represents only the reaction degree of the amorphous component in WBFA (38.5% wt.). Still, it should be noted that this calculation is only suitable for qualitative interpretation rather than quantitative evaluation due to the assumption of $Q_{max,slag}$, and $Q_{max,WBFA}$. Changes in these values will affect the final maximum reaction degrees of WBFA and BFS, respectively.

4.2. Thermodynamic modelling

With the information in Fig. 17, it is possible to predict the phase compositions of the binary pastes using thermodynamic modelling.

Fig. 18 provides the time-dependent phase evolution of binary pastes. It is noteworthy that the (partial) reactive phases originating from WBFA, such as calcite, portlandite, syngenite, and sylvite, are directly used as inputs in the modelling based on the QXRD results. According to the modelling output the main reaction products include C-(A)-S-H gels, ettringite, Fridel's salt, and hydrotalcite, which are in good agreement with the experimental results obtained from XRD and FTIR analyses. Meanwhile, the time-dependent modelling further illustrates the reaction processes of mixtures with different WBFA contents. Mixtures containing higher amounts of WBFA exhibit slower early reactions of both BFS and WBFA and early hydrates formation, but show a more sustained and pronounced reaction at later stages. For instance, in B30S70, clear hydrate formation is observed at early stage, while the generation of hydrates becomes relatively stable after approximately 30 h with a slow rate of increase. In contrast, B50S50 and B70S30 display slower early hydrate formation; however, their cumulative hydrate formation becomes more significant at later stages.

As illustrated earlier, considering the assumptions made in the kinetics calculation, it is challenging to quantitatively analyse the reaction products. Still, the changes in hydrates between the mixtures with different WBFA/BFS ratios can provide insightful information on how the phase evolutions with compositions. As shown, a higher content of WBFA eventually leads to an increased amount of Friedel's salt, as chloride originating from WBFA is largely bound in the hydrates. Meanwhile, the modelling indicates that B50S50 contains the largest amount of ettringite, C-(A)-S-H gels, and hydrotalcite. These hydrates

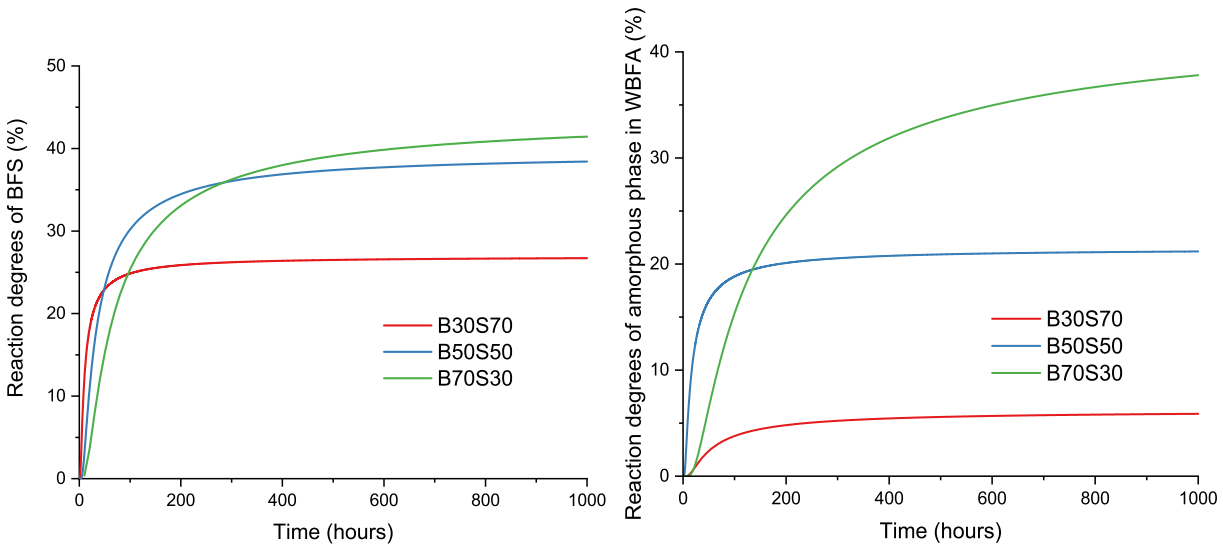

Fig. 17. Calculated reaction degree evolution of BFS and amorphous phase of WBFA.

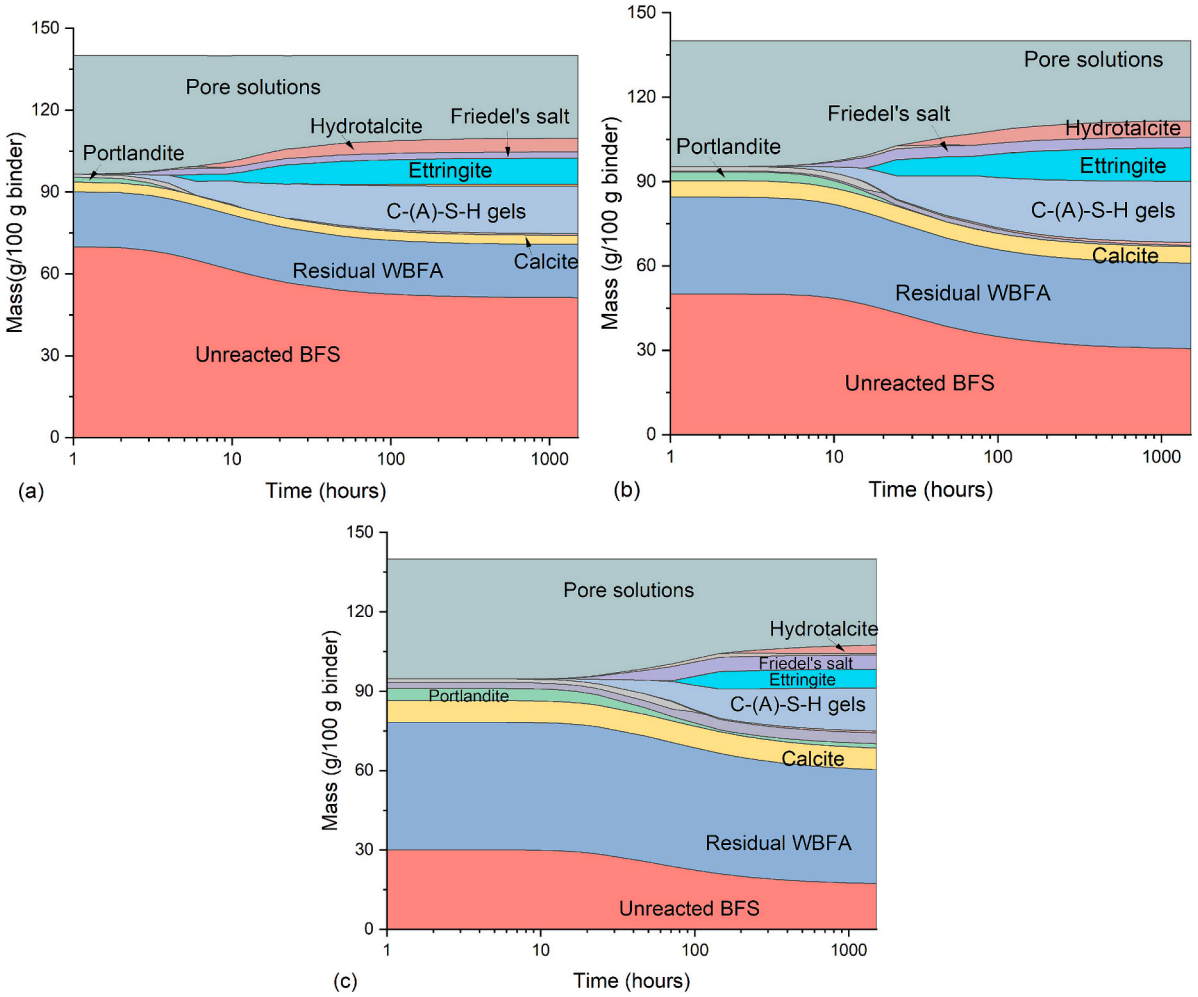

Fig. 18. Thermodynamics modelling of phase evolution of binary pastes over time (a: B30S70, b: B50S50, c: B70S30).

contribute significantly to its strength development, which partly supports the highest compressive strength. By further increasing the content of WBFA to B70S30, however, the amount of hydrates is slightly reduced due to the limited amount of reacted BFS. A synergistic effect between WBFA and BFS is therefore evident.

5. Conclusion

This paper investigated the reaction kinetics and microstructure development of WBFA-BFS binary pastes, validating that WBFA can be used to enhance the reaction of aluminosilicates, demonstrating a synergistic effect with BFS during hydration. Based on the results, the following conclusions are obtained:

1) The combination of BFS, WBFA, and water leads to an intense 'cement hydration-like' exothermic reaction, implying the precipitation of reaction products. Mixtures with a lower WBFA/BFS ratio exhibit more intensive hydrations during the early hydration. Increasing the amount of WBFA benefits BFS hydration in the long term. In the binary pastes, WBFA not only acts as an activator for GGBFS hydration by providing an alkaline and sulphate-rich environment, but also participates directly in the reaction through the gradual dissolution of its reactive amorphous phases, thereby further enhancing the overall reaction.
2) The primary hydration products in the binary pastes are C-S-H gels, ettringite, Friedel's salt, and hydrotalcite. The hydrate compositions are influenced by WBFA/BFS ratios, with hydrotalcite preferentially forming in mixtures with lower WBFA/BFS ratios, and ettringite preferentially forming in mixtures with higher WBFA/BFS ratios.
3) Among the three mixtures, B50S50 appears to be the optimal composition in terms of both reaction behaviour and compressive strength. Compared with B30S70 and B70S30, B50S50 maintains a sustained reaction rate while generating the largest amount of hydrates, as evidenced by the bound water content and thermodynamic modelling. This ultimately leads to the lowest porosity and a more refined microstructure over time, which supports its highest compressive strength among the three mixtures.
4) The binary pastes have a highly porous microstructure, with porosities ranging from 30% to 45%. Longer curing leads to a reduction in porosities. The volume of medium and large capillary pores decreases while the volume of micro capillary pores increases with the refinement of the pore structure.

Due to the intrinsic reaction process and slow strength development, it is expected that the application of WBFA-BFS binary pastes is suitable for low and moderate-strength demanding products. To further extend the recycling approach and improve utilization efficiency, integrating WBFA into composite cement can be considered, which remains a topic for future research.

CRediT authorship contribution statement

Xuhui Liang: Writing – review & editing, Writing – original draft, Methodology, Investigation, Formal analysis, Conceptualization. **Jiayi Chen:** Software, Formal analysis. **Hua Dong:** Writing – review & editing, Supervision. **Zhenming Li:** Writing – review & editing. **Chen Liu:** Writing – review & editing, Formal analysis. **Guang Ye:** Writing – review & editing, Supervision, Resources, Funding acquisition.

Declaration of competing interest

The authors declare that they have no known competing financial interests or personal relationships that could have appeared to influence the work reported in this paper.

Acknowledgment

Xuhui Liang would like to acknowledge the financial supports from the China Scholarship Council (201806050051) and Renewi Mineralz & Water. Zhenming Li would like to acknowledge the Shenzhen Science and Technology Program (KQTD20210811090112003) and National Natural Science Foundation of China (Grant No. 52578274).

Appendix A

Table A1
Chemical compositions of amorphous phase in WBFA [12].

	SiO_2	Al_2O_3	CaO	Fe_2O_3	SO_3	MgO	K_2O	Others	Sum (g/100 g ash)
Treated WBFA	4.18	3.45	20.86	1.06	0.55	2.18	1.91	3.87	38.06

Owing to the complexity of WBFA's mineral compositions, the selective dissolution method [69] commonly used to measure the reaction degree of BFS is not applicable to determine the reaction degrees of BFS in the WBFA-BFS binary pastes. Instead, an image analysis technique was employed. However, it is challenging to directly use greyscale to distinguish the regions of BFS and WBFA, as WBFA contains a wide range of greyscales intensities due to its compositional heterogeneity. Therefore, a modified image analysis technique was adopted, combining EDS mapping, analysis of average elemental ratios in each particle, and greyscales evaluation. For each picture, 50 frames of mapping were captured to ensure reliable results.

The schematic for determining the reaction degree of BFS is presented in Fig. A1. Firstly, based on the BSE images (Fig. A1(a)), the Mg mapping (Fig. A1(b)) was used to define the original boundary of BFS grains, as Mg is typically remain stable during the reaction of BFS [56,70]. By overlapping the Mg mapping onto the BSE image, an overestimation of BFS particles was observed (Fig. A1(c)), owing to the heterogeneous distribution of Mg in WBFA particles.

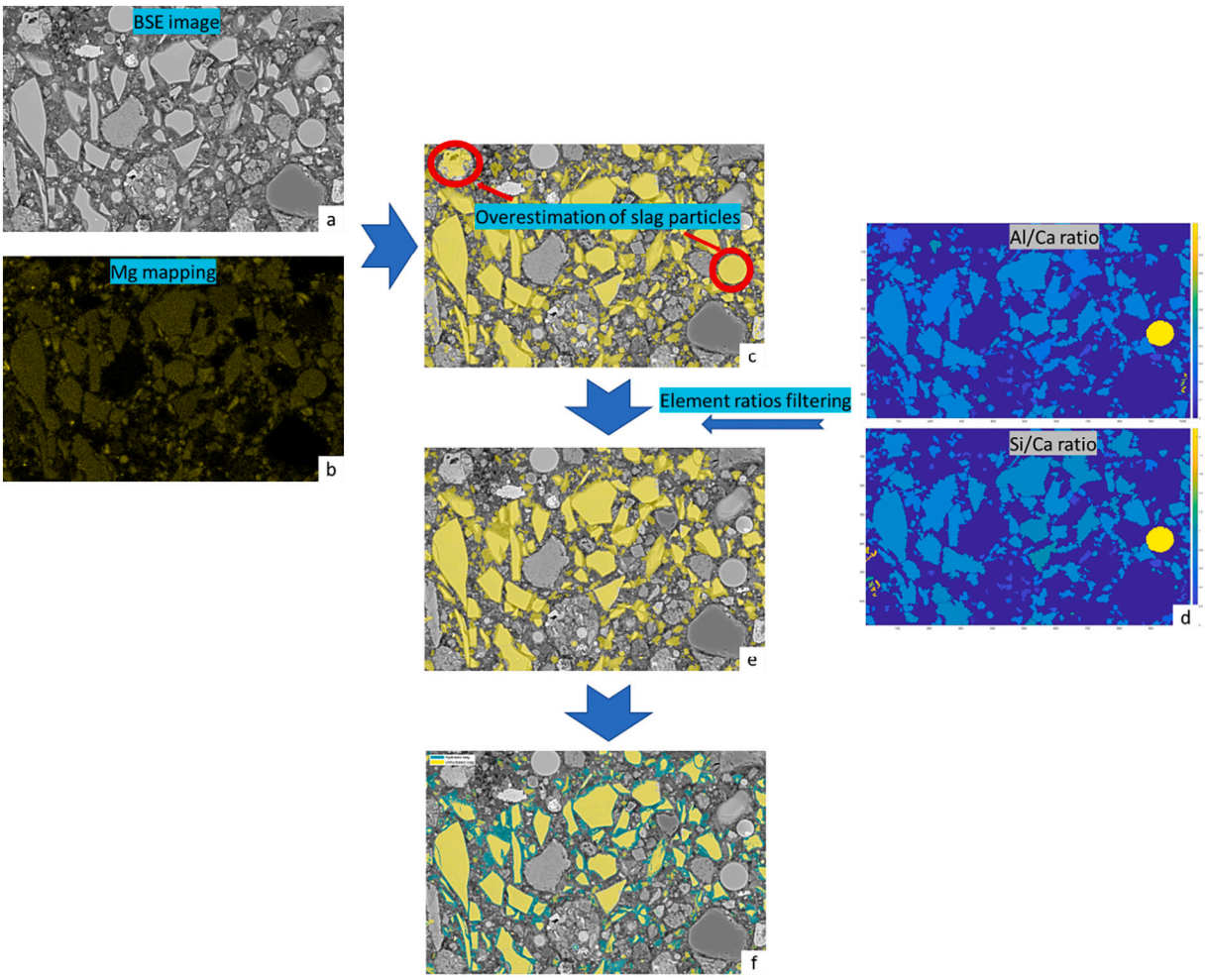

Fig. A1. Schematic diagrams of analysing the reaction degree of BFS by BSE-EDS mapping.

To eliminate Mg-containing WBFA particles, an elemental ratio evaluation was performed individually for each Mg-containing particle, as illustrated in the heatmap (Fig. A1(d)). Mg-bearing WBFA particles exhibited either extremely low or high Si/Ca and Al/Ca ratios compared with BFS particles. Therefore, these WBFA particles were excluded from the analysis (Fig. A1(e)), resulting in a well-defined BFS boundary. Hydrated regions were subsequently segmented based on grayscale variations within the selected particles, where hydrated areas typically appeared as dark grey [66]. The reaction degree of BFS was then calculated with Eq. A1.

$$DoR\ Slag = \frac{Hydrated\ slag\ area}{Total\ slag\ area} \times 100\% \tag{A1}$$

The resolution of the mapping was 203.32 nm/pixel, with a domain size of 628 × 1024 pixels. It is suggested that a surface area of 4.0–5.0 × 10^5 μm^2 be analysed for BSE image analysis to ensure representativeness [71]. Therefore, about 15 EDS mappings were conducted for each sample to ensure the representativeness of the results. This required a total of approximately 8 h per sample.

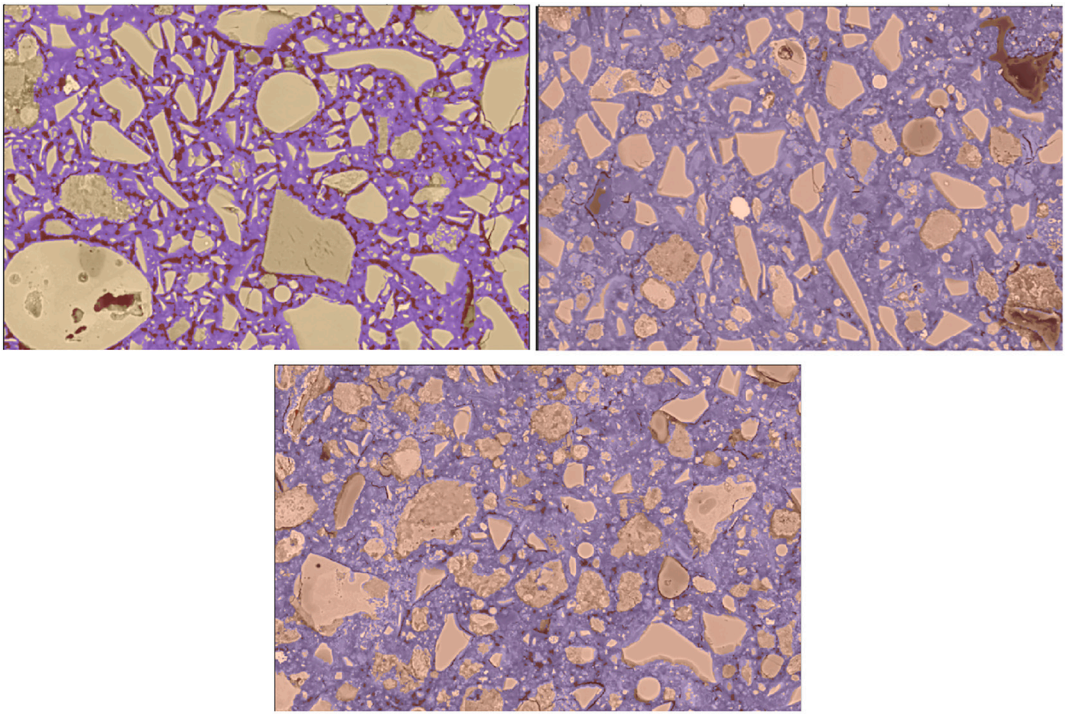

Fig. A2. Phase segmentation of binary pastes at 60 days (The red area indicates the pores and cracks, yellow area indicates the anhydrous particles, purple area indicates the reaction products in the matrix). (For interpretation of the references to colour in this figure legend, the reader is referred to the web version of this article.)

Table A2
Comparison of values Q in binary pastes from Exponential equation and Knudsen's equation.

	Exponential equation	Knudsen's equation
B30S70	85.57 J/g	86.81 J/g
B50S50	120.8 J/g	126.29 J/g
B70S30	168.55 J/g	164.83 J/g

Table A3
Calculated value Q for BFS and WBFA in binary pastes by Knudsen's equation.

	Q_{BFS}	Q_{WBFA}	Q_{Binder}
B30S70	79.17	6.76	85.93
B50S50	82.98	38.94	121.92
B70S30	55.65	110.31	165.96

In Table A3, the enthalpy of binder can be calculated by Eq. A2.

$$Q_{binder} = Q_{BFS} + Q_{WBFA} \quad (A2)$$

It is seen that the calculated Q_{binder} is comparable to that calculated directly from the Knudsen's equation calculated from the total heat from the isothermal calorimetry results. This indicates a well-satisfied result for determining the value of Q_{BFS} and Q_{WBFA}.

Data availability

Data will be made available on request.

References

[1] E. Commission, J.R. Centre, A. Camia, J. Giuntoli, R. Jonsson, N. Robert, N. Cazzaniga, G. Jasinevičius, V. Avitabile, G. Grassi, J. Barredo, S. Mubareka, The Use of Woody Biomass for Energy Production in the EU, Publications Office, 2021, https://doi.org/10.2760/831621.

[2] Eurostat, Complete Energy Balances, n.d. doi:https://doi.org/10.2908/NRG_BAL_C.

[3] B. Hektor, S. Backéus, K. Andersson, Carbon balance for wood production from sustainably managed forests, Biomass Bioenergy 93 (2016) 1–5, https://doi.org/10.1016/j.biombioe.2016.05.025.

[4] P. Lauri, P. Havlík, G. Kindermann, N. Forsell, H. Böttcher, M. Obersteiner, Woody biomass energy potential in 2050, Energy Policy 66 (2014) 19–31, https://doi.org/10.1016/j.enpol.2013.11.033.

[5] C. Sulaiman, A.S. Abdul-Rahim, C.A. Ofozor, Does wood biomass energy use reduce CO2 emissions in european union member countries? Evidence from 27 members, J. Clean. Prod. 253 (2020) 119996, https://doi.org/10.1016/j.jclepro.2020.119996.

[6] J. Zhai, I.T. Burke, D.I. Stewart, Beneficial management of biomass combustion ashes, Renew. Sust. Energ. Rev. 151 (2021) 111555, https://doi.org/10.1016/j.rser.2021.111555.
[7] X. Liang, Z. Li, H. Dong, G. Ye, A review on the characteristics of wood biomass fly ash and their influences on the valorization in cementitious materials, J. Build. Eng. 97 (2024) 110927, https://doi.org/10.1016/j.jobe.2024.110927.
[8] R. Rajamma, R.J. Ball, L.A.C. Tarelho, G.C. Allen, J.A. Labrincha, V.M. Ferreira, Characterisation and use of biomass fly ash in cement-based materials, J. Hazard. Mater. 172 (2009) 1049–1060, https://doi.org/10.1016/j.jhazmat.2009.07.109.
[9] M. Berra, T. Mangialardi, A.E. Paolini, Reuse of woody biomass fly ash in cement-based materials, Constr. Build. Mater. 76 (2015) 286–296, https://doi.org/10.1016/j.conbuildmat.2014.11.052.
[10] I. Carević, A. Baričević, N. Štirmer, J. Šantek Bajto, Correlation between physical and chemical properties of wood biomass ash and cement composites performances, Constr. Build. Mater. 256 (2020) 119450, https://doi.org/10.1016/j.conbuildmat.2020.119450.
[11] M.E. Küçük, T. Kinnarinen, A. Häkkinen, Dissolution kinetics of aluminosilicates from biomass ashes in alkaline solutions, Ceram. Int. 47 (2021) 11714–11726, https://doi.org/10.1016/J.CERAMINT.2021.01.011.
[12] X. Liang, H. Dong, Z. Li, C. Liu, S. Zhang, G. Ye, Characterization, pretreatment, and valorization of wood biomass fly ash in a binary cement-free binder, Dev. Built Environ. 23 (2025) 100700, https://doi.org/10.1016/j.dibe.2025.100700.
[13] R. Rajamma, J.A. Labrincha, V.M. Ferreira, Alkali activation of biomass fly ash-metakaolin blends, Fuel 98 (2012) 265–271, https://doi.org/10.1016/j.fuel.2012.04.006.
[14] R. Kaminskas, V. Cesnauskas, R. Kubiliute, Influence of biomass fly ash additive on blast-furnace cement hydration and hardening, Adv. Cem. Res. 29 (2017) 313–321, https://doi.org/10.1680/jadcr.16.00190.
[15] T.H. Silva, L.F.S. Lara, G.J.B. Silva, J.L. Provis, A.C.S. Bezerra, Alkali-activated materials produced using high-calcium, high-carbon biomass ash, Cem. Concr. Compos. 132 (2022) 104646, https://doi.org/10.1016/j.cemconcomp.2022.104646.
[16] S.V. Vassilev, D. Baxter, L.K. Andersen, C.G. Vassileva, An overview of the composition and application of biomass ash. Part 1. Phase-mineral and chemical composition and classification, Fuel 105 (2013) 40–76, https://doi.org/10.1016/j.fuel.2012.09.041.
[17] S. Jurado-Contreras, E. Bonet-Martínez, P.J. Sánchez-Soto, O. Gencel, D. Eliche-Quesada, Synthesis and characterization of alkali-activated materials containing biomass fly ash and metakaolin: effect of the soluble salt content of the residue, Arch. Civ. Mech. Eng. 22 (2022) 1–21, https://doi.org/10.1007/s43452-022-00444-2.
[18] I. Salas, E. Cifrian, L. Soriano, J. Monzó, A. Andrés, Environmental assessment of alkali-activated materials based on agro-industrial waste as alkaline activators through leaching tests, J. Environ. Manag. 368 (2024) 122265, https://doi.org/10.1016/j.jenvman.2024.122265.
[19] J. Fořt, M. Mildner, M. Keppert, M. Abed, R. Černý, Potential of industrial waste as alternative alkaline activator for development of eco-efficient mortars, Case Stud. Constr. Mater. 18 (2023) e01716, https://doi.org/10.1016/j.cscm.2022.e01716.
[20] K. Sun, H.A. Ali, D. Xuan, J. Ban, C.S. Poon, Utilization of APC residues from sewage sludge incineration process as activator of alkali-activated slag/glass powder material, Cem. Concr. Compos. 133 (2022) 104680, https://doi.org/10.1016/j.cemconcomp.2022.104680.
[21] S.V. Vassilev, D. Baxter, L.K. Andersen, C.G. Vassileva, An overview of the composition and application of biomass ash. Part 1. Phase-mineral and chemical composition and classification, Fuel 105 (2013) 40–76, https://doi.org/10.1016/j.fuel.2012.09.041.
[22] R.S. Barneyback, S. Diamond, Expression and analysis of pore fluids from hardened cement pastes and mortars, Cem. Concr. Res. 11 (1981) 279–285, https://doi.org/10.1016/0008-8846(81)90069-7.
[23] C. Dehghanian, M. Arjemandi, Influence of slag blended cement concrete on chloride diffusion rate, Cem. Concr. Res. 27 (1997) 937–945, https://doi.org/10.1016/S0008-8846(97)00064-1.
[24] P.S. Mangat, J.M. Khatib, B.T. Molloy, Microstructure, chloride diffusion and reinforcement corrosion in blended cement paste and concrete, Cem. Concr. Compos. 16 (1994) 73–81, https://doi.org/10.1016/0958-9465(94)90002-7.
[25] R. Snellings, J. Chwast, Ö. Cizer, N. De Belie, Y. Dhandapani, P. Durdzinski, J. Elsen, J. Haufe, D. Hooton, C. Patapy, M. Santhanam, K. Scrivener, D. Snoeck, L. Steger, S. Tongbo, A. Vollpracht, F. Winnefeld, B. Lothenbach, RILEM TC-238 SCM recommendation on hydration stoppage by solvent exchange for the study of hydrate assemblages, Mater. Struct. Constr. 51 (2018), https://doi.org/10.1617/s11527-018-1298-5.
[26] E.W. Washburn, Note on a method of determining the distribution of pore sizes in a porous material, Proc. Natl. Acad. Sci. 7 (1921) 115–116, https://doi.org/10.1073/pnas.7.4.115.
[27] H.S. Wong, M.K. Head, N.R. Buenfeld, Pore segmentation of cement-based materials from backscattered electron images, Cem. Concr. Res. 36 (2006) 1083–1090, https://doi.org/10.1016/j.cemconres.2005.10.006.
[28] K. Scrivener, R. Snellings, B. Lothenbach, A practical guide to microstructural analysis of cementitious materials, CRC Press (2018), https://doi.org/10.1201/b19074.
[29] Z. Li, T. Lu, X. Liang, H. Dong, J. Granja, M. Azenha, G. Ye, Mechanisms of autogenous shrinkage of alkali-activated slag and fly ash pastes, Cem. Concr. Res. 135 (2020), https://doi.org/10.1016/j.cemconres.2020.106107.
[30] M. Chabannes, H. Kazemi-kamyab, J. Trigallez, R. Snellings, Performance and microstructure development of lime – calcined fluvial sediment binders under different curing conditions, Cem. Concr. Res. 160 (2022) 106903, https://doi.org/10.1016/j.cemconres.2022.106903.
[31] A. Schöler, B. Lothenbach, F. Winnefeld, M. Ben Haha, M. Zajac, H.M. Ludwig, Early hydration of SCM-blended Portland cements: a pore solution and isothermal calorimetry study, Cem. Concr. Res. 93 (2017) 71–82, https://doi.org/10.1016/J.CEMCONRES.2016.11.013.
[32] S. Adu-Amankwah, L. Black, J. Skocek, M. Ben Haha, M. Zajac, Effect of sulfate additions on hydration and performance of ternary slag-limestone composite cements, Constr. Build. Mater. 164 (2018) 451–462, https://doi.org/10.1016/j.conbuildmat.2017.12.165.
[33] D. Jansen, F. Goetz-Neunhoeffer, C. Stabler, J. Neubauer, A remastered external standard method applied to the quantification of early OPC hydration, Cem. Concr. Res. 41 (2011) 602–608, https://doi.org/10.1016/j.cemconres.2011.03.004.
[34] H. Nguyen, P. Kinnunen, K. Gijbels, V. Carvelli, H. Sreenivasan, A.M. Kantola, V. V. Telkki, W. Schroeyers, M. Illikainen, Ettringite-based binder from ladle slag and gypsum – the effect of citric acid on fresh and hardened state properties, Cem. Concr. Res. 123 (2019) 105800, https://doi.org/10.1016/j.cemconres.2019.105800.
[35] T. Wagner, D.A. Kulik, F.F. Hingerl, S.V. Dmytrieva, GEM-SELEKTOR GEOCHEMICAL MODELING PACKAGE: TSolMod LIBRARY AND DATA INTERFACE FOR MULTICOMPONENT PHASE MODELS, Can. Mineral. 50 (2012) 1173–1195, https://doi.org/10.3749/canmin.50.5.1173.
[36] D.A. Kulik, T. Wagner, S.V. Dmytrieva, G. Kosakowski, F.F. Hingerl, K. V. Chudnenko, U.R. Berner, GEM-Selektor geochemical modeling package: revised algorithm and GEMS3K numerical kernel for coupled simulation codes, Comput. Geosci. 17 (2013) 1–24, https://doi.org/10.1007/s10596-012-9310-6.
[37] B. Lothenbach, D.A. Kulik, T. Matschei, M. Balonis, L. Baquerizo, B. Dilnesa, G. D. Miron, R.J. Myers, Cemdata18: a chemical thermodynamic database for hydrated Portland cements and alkali-activated materials, Cem. Concr. Res. 115 (2019) 472–506, https://doi.org/10.1016/j.cemconres.2018.04.018.
[38] B. Lothenbach, Thermodynamic equilibrium calculations in cementitious systems, Mater. Struct. 43 (2010) 1413–1433, https://doi.org/10.1617/s11527-010-9592-x.
[39] D. Rothstein, J.J. Thomas, B.J. Christensen, H.M. Jennings, Solubility behavior of ca-, s-, al-, and si-bearing solid phases in Portland cement pore solutions as a function of hydration time, Cem. Concr. Res. 32 (2002) 1663–1671, https://doi.org/10.1016/S0008-8846(02)00855-4.
[40] X. Li, J. Bizzozero, C. Hesse, Impact of C-S-H seeding on hydration and strength of slag blended cement, Cem. Concr. Res. 161 (2022) 106935, https://doi.org/10.1016/j.cemconres.2022.106935.
[41] Z. Shi, M.R. Geiker, B. Lothenbach, K. De Weerdt, S.F. Garzón, K. Enemark-Rasmussen, J. Skibsted, Friedels salt profiles from thermogravimetric analysis and thermodynamic modelling of Portland cement-based mortars exposed to sodium chloride solution, Cem. Concr. Compos. 78 (2017) 73–83, https://doi.org/10.1016/j.cemconcomp.2017.01.002.
[42] M. Balonis, B. Lothenbach, G. Le Saout, F.P. Glasser, Impact of chloride on the mineralogy of hydrated Portland cement systems, Cem. Concr. Res. 40 (2010) 1009–1022, https://doi.org/10.1016/j.cemconres.2010.03.002.
[43] K. De Weerdt, H. Justnes, The effect of sea water on the phase assemblage of hydrated cement paste, Cem. Concr. Compos. 55 (2015) 215–222, https://doi.org/10.1016/j.cemconcomp.2014.09.006.
[44] S.-D. Wang, K.L. Scrivener, Hydration products of alkali activated slag cement, Cem. Concr. Res. 25 (1995) 561–571, https://doi.org/10.1016/0008-8846(95)00045-E.
[45] Y. Mohassab, H.Y. Sohn, Analysis of slag chemistry by FTIR-RAS and raman spectroscopy: effect of water vapor content in H2-H2O-CO-CO2 mixtures relevant to a novel green ironmaking technology, Steel Res. Int. 86 (2015) 740–752, https://doi.org/10.1002/srin.201400186.
[46] I. García-Lodeiro, A. Fernández-Jiménez, M.T. Blanco, A. Palomo, FTIR study of the sol-gel synthesis of cementitious gels: C-S-H and N-A-S-H, J. Sol-Gel Sci. Technol. 45 (2008) 63–72, https://doi.org/10.1007/s10971-007-1643-6.
[47] C. Liu, Z. Li, G. Ye, Mechanisms of efflorescence of alkali-activated slag, Cem. Concr. Compos. 155 (2025) 105811, https://doi.org/10.1016/j.cemconcomp.2024.105811.
[48] P. Yu, R.J. Kirkpatrick, B. Poe, P.F. McMillan, X. Cong, Structure of calcium silicate hydrate (C-S-H): near-, mid-, and far-infrared spectroscopy, J. Am. Ceram. Soc. 48 (1999) 742–748.
[49] L. Pérez-Villarejo, E. Bonet-Martínez, D. Eliche-Quesada, P.J. Sánchez-Soto, J. M. Rincón-López, E. Castro-Galiano, Biomass fly ash and aluminium industry slags-based geopolymers, Mater. Lett. 229 (2018) 6–12, https://doi.org/10.1016/j.matlet.2018.06.100.
[50] E. Scholtzová, L. Kucková, J. Kožíšek, D. Tunega, Structural and spectroscopic characterization of ettringite mineral –combined DFT and experimental study, J. Mol. Struct. 1100 (2015) 215–224, https://doi.org/10.1016/J.MOLSTRUC.2015.06.075.
[51] J.L. García Fernández, M.C. Alonso Calvo, Ordinary Portland cement composition for the optimization of the synergies of supplementary cementitious materials of ternary binders in hydration processes, Cem. Concr. Compos. 89 (2018) 238–250, https://doi.org/10.1016/J.CEMCONCOMP.2017.12.016.
[52] B. Lothenbach, E. Wieland, A thermodynamic approach to the hydration of sulphate-resisting Portland cement, Waste Manag. 26 (2006) 706–719, https://doi.org/10.1016/j.wasman.2006.01.023.
[53] Z.-L. Jiang, Y.-J. Pan, J.-F. Lu, Y. Wang, Pore structure characterization of cement-based materials by different experimental methods and its influence on permeability evaluation, Cem. Concr. Res. 159 (2022) 106892, https://doi.org/10.2139/ssrn.4019251.

[54] P. Kumar Mehta, Paulo J.M. Monteiro, Concrete: microstructure, properties, and materials, McGraw-Hill Publishing, 2006, pp. 30–32.
[55] D.A. Silva, V.M. John, J.L.D. Ribeiro, H.R. Roman, Pore size distribution of hydrated cement pastes modified with polymers, Cem. Concr. Res. 31 (2001) 1177–1184, https://doi.org/10.1016/S0008-8846(01)00549-X.
[56] Y. Zhang, O. Çopuroğlu, Role of the grain size on the hydration characteristics of slag in an aged field concrete, Cem. Concr. Res. 162 (2022), https://doi.org/10.1016/j.cemconres.2022.106985.
[57] S. Igarashi, M. Kawamura, A. Watanabe, Analysis of cement pastes and mortars by a combination of backscatter-based SEM image analysis and calculations based on the powers model, Cem. Concr. Compos. 26 (2004) 977–985, https://doi.org/10.1016/j.cemconcomp.2004.02.031.
[58] M.H.N. Yio, J.C. Phelan, H.S. Wong, N.R. Buenfeld, Determining the slag fraction, water/binder ratio and degree of hydration in hardened cement pastes, Cem. Concr. Res. 56 (2014) 171–181, https://doi.org/10.1016/j.cemconres.2013.12.002.
[59] F. Georget, W. Wilson, K.L. Scrivener, Edxia: microstructure characterisation from quantified SEM-EDS hypermaps, Cem. Concr. Res. 141 (2021) 106327, https://doi.org/10.1016/j.cemconres.2020.106327.
[60] M. Nedeljković, Z. Li, G. Ye, Setting, strength, and autogenous shrinkage of alkali-activated fly ash and slag pastes: effect of slag content, Materials (Basel) 11 (2018), https://doi.org/10.3390/ma11112121.
[61] X. Hu, C. Shi, Z. Shi, L. Zhang, Compressive strength, pore structure and chloride transport properties of alkali-activated slag/fly ash mortars, Cem. Concr. Compos. (2019), https://doi.org/10.1016/j.cemconcomp.2019.103392.
[62] O. Burciaga-Díaz, Parameters affecting the properties and microstructure of quicklime (CaO) - activated slag cement pastes, Cem. Concr. Compos. 103 (2019) 104–111, https://doi.org/10.1016/J.CEMCONCOMP.2019.05.002.
[63] B. Yuan, Q.L. Yu, H.J.H. Brouwers, Evaluation of slag characteristics on the reaction kinetics and mechanical properties of Na2CO3 activated slag, Constr. Build. Mater. 131 (2017) 334–346, https://doi.org/10.1016/j.conbuildmat.2016.11.074.
[64] A. Schindler, K. Folliard, Heat of hydration models for cementitious materials, ACI Mater. J. 102 (2005) 77–90, https://doi.org/10.14359/14246.
[65] Y. Zuo, M. Nedeljković, G. Ye, Coupled thermodynamic modelling and experimental study of sodium hydroxide activated slag, Constr. Build. Mater. 188 (2018) 262–279, https://doi.org/10.1016/j.conbuildmat.2018.08.087.
[66] V. Kocaba, E. Gallucci, K.L. Scrivener, Methods for determination of degree of reaction of slag in blended cement pastes, Cem. Concr. Res. 42 (2012) 511–525, https://doi.org/10.1016/j.cemconres.2011.11.010.
[67] Y. Sun, Z.H. Wang, D.J. Park, Y.K. Chen, H.S. Kim, W.S. Kim, H.S. Lee, Mathematical determination of the maximum heat release for fly ash cement paste: effect of heat flow monitoring time, calculation approach and fly ash content, Thermochim. Acta 726 (2023) 179553, https://doi.org/10.1016/j.tca.2023.179553.
[68] S. Chithiraputhiran, N. Neithalath, Isothermal reaction kinetics and temperature dependence of alkali activation of slag, fly ash and their blends, Constr. Build. Mater. 45 (2013) 233–242, https://doi.org/10.1016/j.conbuildmat.2013.03.061.
[69] J.S. Lumley, R.S. Gollop, G.K. Moir, H.F.W. Taylor, Degrees of reaction of the slag in some blends with Portland cements, Cem. Concr. Res. 26 (1996) 139–151, https://doi.org/10.1016/0008-8846(95)00190-5.
[70] J.I. Escalante-Garcia, J.H. Sharp, The chemical composition and microstructure of hydration products in blended cements, Cem. Concr. Compos. 26 (2004) 967–976, https://doi.org/10.1016/j.cemconcomp.2004.02.036.
[71] G. Ye, Experimental Study and Numerical Simulation of the Development of the Microstructure and Permeability of Cementitious Materials, 2003.